minerals

MDPI

Article

Formation of Niujuan Ag-Au Deposit, North China Craton: Constraints from Pyrite Textures and In-Situ Trace Element and H-O-S Isotope Geochemistry

Chunlai Liu [1], Ruiming Cao [1,*], Wei Li [2], Xiaoxuan Liu [2], Ke Huang [2], Wei Pan [1], Wei Cui [1] and Linan Cui [1]

[1] The Second Geological Brigade of Hebei Bureau of Geology and Mineral Exploration and Development, Tangshan 063000, China; cuilinan67@163.com (L.C.)
[2] School of Earth Sciences and Resources, China University of Geosciences (Beijing), Beijing 100083, China
* Correspondence: caoruiming2014@163.com

Abstract

The North China Craton (NCC) hosts numerous world-class Au deposits and these Au deposits can be classified into the Au-only and Ag-Au polymetallics, respectively. The former is mostly located in the eastern NCC, such as in the giant Jiaodong Province, and the latter is mostly distributed along the northern and southern margins of the NCC. Compared with Au-only deposits, the ore genesis of the Ag-Au deposits remains controversial. This paper focuses on the Niujuan Ag-Au deposit in the Fengning ore cluster of the northern margin of the NCC. Detailed deposit geology investigation, texture analysis, and analyses of the in situ trace element and sulfur isotope compositions of pyrite, coupled with H-O isotope compositions of quartz from different stages, were conducted to elucidate the ore-forming processes and metal sources. The results showed that the formation of the Niujuan deposit can be divided into four stages, including a pre-ore siliceous breccia stage (stage 1), syn-ore quartz-pyrite stage (stage 2), syn-ore polymetallic sulfide stage (stage 3), and post-ore fluorite-calcite stage (stage 4). Among these, stage 3 represents the major Ag-Au mineralization stage. Pyrite is well developed within stage 2 and stage 3, representing the intensive sulfidation of the wall rock. Microscopic analytical techniques including gamma-enhanced reflected light and scanning electron microscopy backscattered electron (BSE) reveal that pyrite samples from stage 2 and stage 3 have distinct textures. Pyrite (Py1) from stage 2 is homogeneous but with numerous pores. In contrast, pyrite (Py2) from stage 3 has overgrowth textures, and be divided into three sub-stages from core to rim (Py2a, Py2b, and Py2c) with different BSE brightness levels. LA-ICP-MS trace elements analyses results show that these different stages of pyrite show different composition such as Au, As, Ag, Co, and Ni. Py1 has low Au and Ag concentrations ranging from <0.1 ppm to 0.02 ppm and <0.1 ppm to 21.8 ppm, respectively. Py2a has low Au and Ag concentrations ranging from <0.1 ppm to 0.4 ppm and 0.4 ppm to 118.4 ppm, respectively. Py2b is characterized by high As and low Au contents, with average values of 6670.8 ppm for As and 1.4 ppm for Au. Py2c shows relatively low Co and Ni concentrations ranging from 0.02 ppm to 255.2 ppm and <0.1 ppm to 9.9 ppm, respectively. The sulfur isotope composition of Py1 and Py2 is relatively consistent, ranging from 3.8‰ to 6.7‰. The H and O isotope compositions of quartz from stage 1, stage 2, and stage 3 have insignificant variations, ranging from −119.5‰ to −101.3‰ for δD and −6.8‰ to −3.7‰ for $\delta^{18}O_{fluid}$, respectively. The results show that sulfur and, possibly, Au and Ag were mainly derived from magmatic hydrothermal fluids, and a significant amount of meteoric water was involved. Combined with the published mineralizing ages (~140 Ma), this paper suggests that the Niujuan Ag-Au deposit formed during the Early Cretaceous under an extensional setting in response to the eastward retreating subduction of the Paleo-Pacific oceanic plate.

Check for updates

Academic Editor: Pura Alfonso

Received: 11 January 2026
Revised: 12 February 2026
Accepted: 14 February 2026
Published: 28 February 2026

Copyright: © 2026 by the authors. Licensee MDPI, Basel, Switzerland. This article is an open access article distributed under the terms and conditions of the Creative Commons Attribution (CC BY) license.

Evidence from deposit geology and geochemistry reveals that the mixture of magmatic and meteoric water, together with intensive sulfidation, is the key factor controlling Au and Ag deposition.

Keywords: pyrite; in situ trace elements; Niujuan; Ag-Au deposits; North China Craton

1. Introduction

The North China Craton (NCC) is one of the world's most significant Au provinces, hosting several large-scale Au ore clusters, such as in Jiaodong, Liaodong, the Xiaoqinling–Xiong'er Mountains, Eastern–Northern Hebei, the central Taihang Mountains, and the Chifeng–Chaoyang district [1]. Two types of Au deposits have been recognized based on the elemental association, namely Au-only and Ag-Au polymetallic deposits. The former type is widely distributed such as those deposits in Jiaodong Province, and in contrast, the Ag-Au deposits are mostly distributed along the northern and southern margins of the NCC [2]. Except for the metal association difference, these Au and Ag-Au deposits exhibit distinct mineralization ages [3]. Au-only mineralization in the Jiaodong region took place at a relatively narrow interval at 120 ± 5 Ma [4]. In contrast, Ag-Au deposits in the Northern margin of the NCC show a wide range from 400 to 140 Ma [5–7], although precisely dating those deposits still be a challenge due to the lack of suitable minerals. Therefore, elucidating the mineralization processes and ore-forming fluids and materials is crucial for understanding the formation of these Ag-Au deposits. Previous studies have largely focused on Au deposits, particularly those in the Jiaodong region, where detailed microtextural and in situ geochemical investigations of auriferous pyrite using SIMS and LA-ICP-MS have provided robust constraints on ore-forming processes [5,8–15]. These studies have demonstrated that pyrite can record the fluid evolution and Au precipitation mechanisms. In comparation, detailed studies on the formation processes of these Ag-Au deposits using in situ analytical methods remain relatively scarce.

Most Au and Ag-Au deposits around the NCC are hosted within Precambrian metamorphic rocks and Paleozoic–Mesozoic igneous rocks. The genesis of Au and Ag-Au deposits in the NCC remains highly controversial. For Jiaodong-type Au deposits, the prevailing genetic model attributes their formation primarily to magmatic hydrothermal processes related to Mesozoic magmatism [16–21], whereas alternative models emphasize a metamorphic fluid source [22–25]. In the case of the Niujuan Ag-Au deposit, there are also different interpretations for its origin, including metamorphic fluids and magmatic and meteoric water models [26,27].

This paper focuses on the Niujuan Ag-Au deposit in the Fengning ore cluster at the northern margin of the NCC (?). Based on detailed field geological investigations and microtextural observations, we conducted the in situ laser ablation (multi-collector)–inductively coupled plasma mass spectrometry (LA-(MC)-ICP-MS) analysis of pyrite to investigate the content of invisible Au and associated trace elements, and in situ S isotopes, coupled with analysing the H-O isotope compositions of quartz from different stages, to document the ore-forming processes and sources of fluid and materials. By integrating these new data, this contribution aims to unveil the formation mechanism of the Niujuan Ag-Au deposit and to provide new insights into the formation mechanisms of Ag-Au and Au mineralization in the NCC.

2. Geological Setting

2.1. Regional Geology

The NCC is composed of two strata units: the Archean-to-Early-Proterozoic metamorphic basement complexes and the Proterozoic, the Paleozoic, the Mesozoic, and the Cenozoic sedimentary cover rocks [28] (Figure 1A). The Archean-to-Early-Paleoproterozoic high-grade metamorphic basement is dominated by mafic granulite, amphibolite, gneiss, magnetite quartzite, marble, and charnockite [29–33]. The Proterozoic-to-Cenozoic sedimentary sequences consist of sandstone, conglomerate, coal-bearing shale, clastic deposits, and carbonate rocks [32]. The exposed strata in the Fengning Ag-polymetallic ore district are dominated by the Paleoproterozoic in age, with subordinate Mesozoic strata and Quaternary sediments occurring sporadically. The Paleoproterozoic strata is a set of volcanic sedimentary rocks with low amphibolite facies, and mainly comprises granulite, including graphite-rich granulite, amphibolite, quartzite, and marble assemblages [34]. The Mesozoic strata are predominantly composed of Jurassic granite, all of which exhibit a close genetic association with large-scale mineralization in this region.

The Fengning Ag-Au polymetallic ore cluster is geologically characterized by intensive faulting structures and extensive magmatic activities. The region experienced Late Neoarchean–Proterozoic subduction, collision, and extension-related orogenic processes along an active continental margin, followed by multiple Mesozoic tectonic events, including the NCC reactivation, lithospheric thinning, and intracontinental orogeny [35]. The exposed igneous rocks in the region primarily include the Triassic granite and the Jurassic granite. The Triassic granite yields a zircon U-Pb age of 268.7 ± 3.2 Ma. The Jurassic granite has zircon U-Pb ages of 254.2 ± 2.8 Ma, occurring primarily as dikes [36].

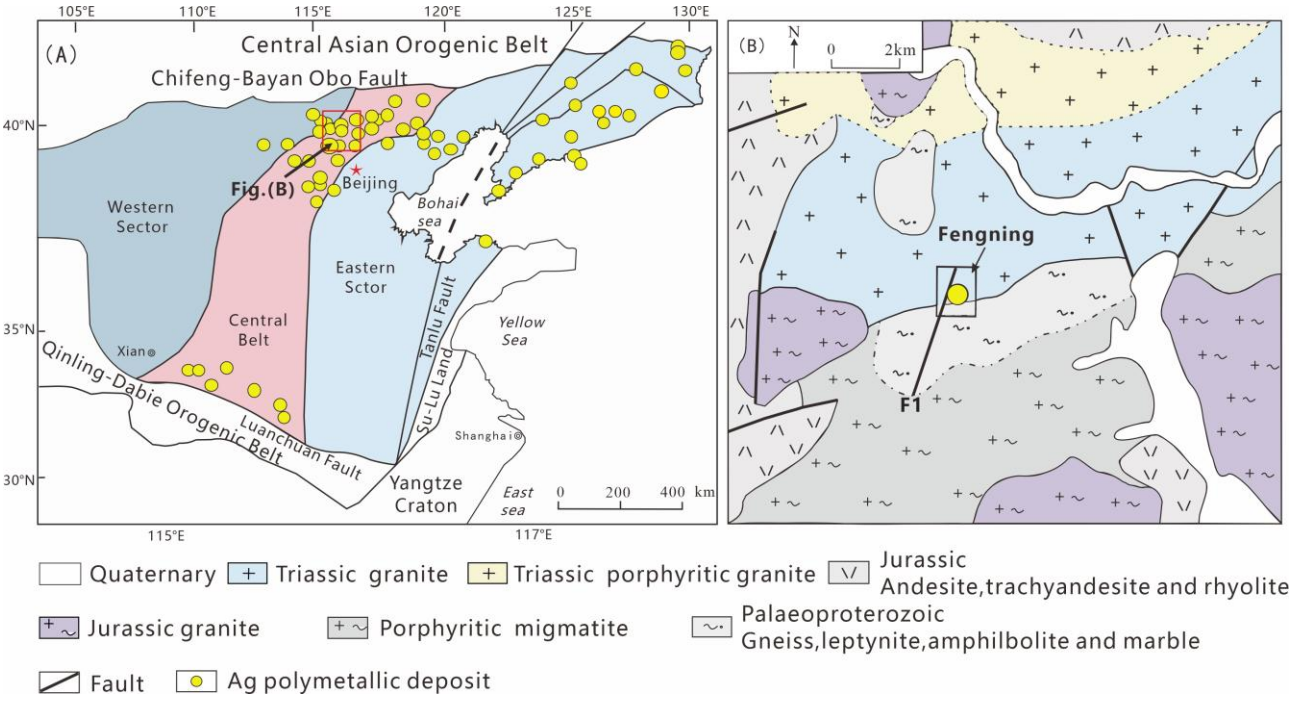

Figure 1. (**A**) Sketch map of the NCC showing the distribution Ag-Au polymetallic ore deposits (modified after [37]). (**B**) Regional geological map of the Fengning Ag-polymetallic ore cluster (modified after [38]).

Ag-Au polymetallic deposits in the Fengning Ag-Au polymetallic ore cluster are widespread. These deposits are predominantly controlled by the Niujuan–Laohuba Fault, a secondary fault of the Shanghuangqi–Wulonggou Fault Zone, which is also named the F1

Fault (Figure 1B). The F1 Fault represents the main ore-controlling structure of the Fengning Ag-polymetallic ore cluster, striking 25–35° and dipping southeast [39].

2.2. Deposit Geology

The Niujuan Ag-Au deposit, situated in the Fengning ore cluster, consists of 26 orebodies (Figure 2), of which the shallow orebodies have been mined whereas the newly discovered deep orebodies remain unexploited. Ore bodies are predominantly hosted in the F1 fault zone, a secondary structure subordinate to the regional NNE-striking fault and characterized by the occurrence of intense fracturing breccia. In the shallow mineralization zone, No. I and II represent the main ore bodies. Orebody No. I contains Ag and Au grades of 159–747 g/t (average 517 g/t) and 0.41–3.85 g/t (average 1.95 g/t), respectively. Orebody No. II has Ag and Au grades ranging from 125 to 810 g/t (average 608 g/t) and 1.2 to 3.87 g/t (average 1.90 g/t), respectively [39]. The orebody No. I generally strikes NNE and dips SE, with a thickness ranging from 1 to 18 m (average 8.02 m) and a maximum strike length of 410 m. The orebody No. II is parallel to the No. I orebody, extending approximately 165 m along strike with a surface thickness of 2–5.9 m (average 3.3 m) [40]. The unexposed orebody No. III is the main orebody in the deep part, having the highest ore grade. It strikes northeast and a dip of 48–55°. The minimum thickness revealed by drilling is 0.52 m, and the maximum is 27.71 m.

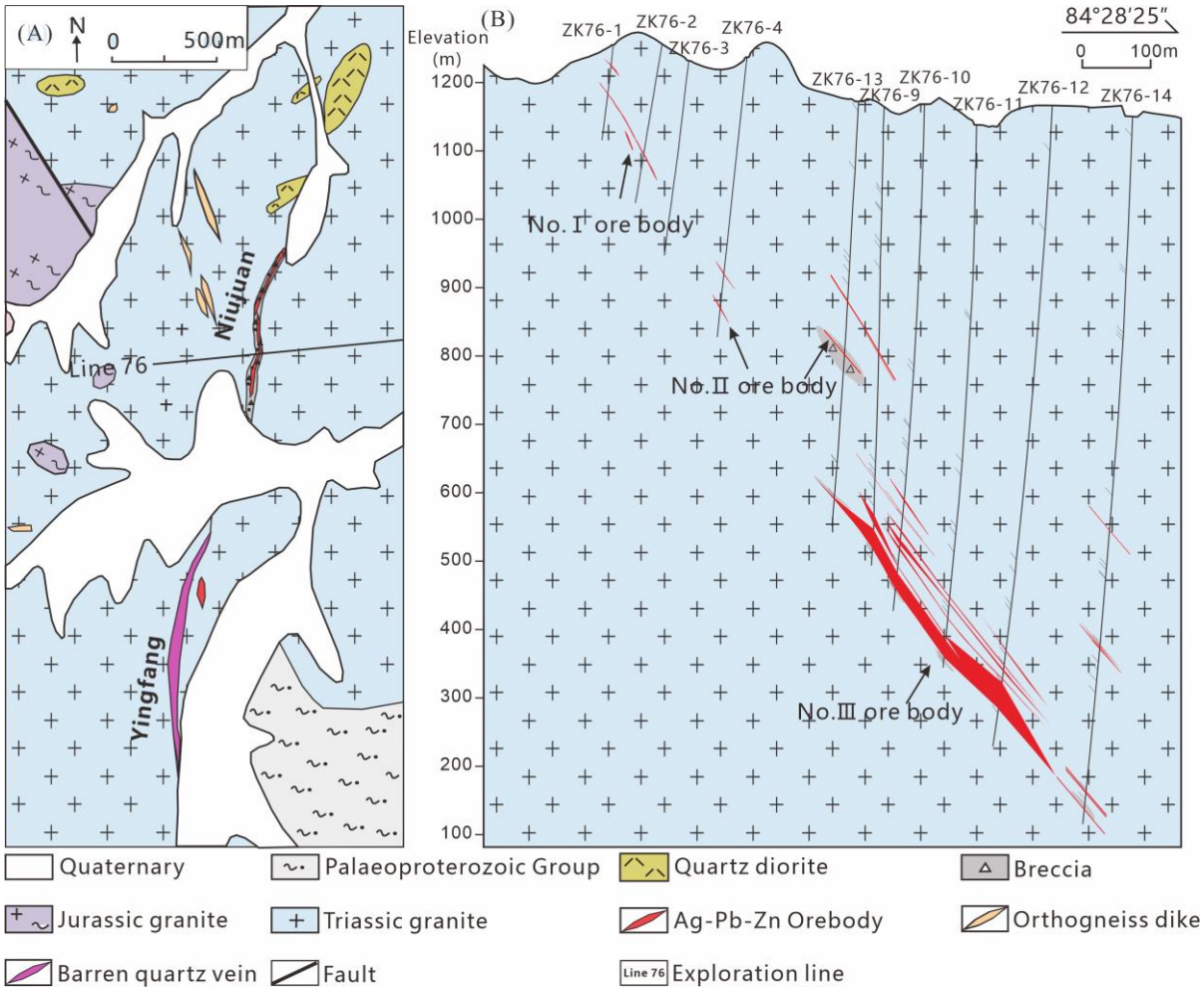

Figure 2. (**A**) Geological map of the Niujuan Ag-Au deposit (modified after [37]). (**B**) Geological cross-section of exploration line 76 showing the shallow and deep orebodies.

The strata exposed in the Niujuan Ag-Au Deposit consist of Paleoproterozoic metamorphic rocks and Mesozoic granites. The Paleoproterozoic metamorphic rocks include graphite-bearing biotite plagioclase gneiss, garnet-bearing biotite plagioclase gneiss, amphibolite, migmatitic gneiss, and marble. These metamorphic rocks have been intruded by biotite monzonitic granite of Triassic age and biotite K-feldspar granite of Jurassic age, as well as some felsic and diabase dykes [36].

Ag-Au orebodies are mainly hosted in the Triassic biotite monzogranite (Figure 2). The host rocks develop intensive hydrothermal alteration, including silicification, K-feldspar alteration, sericitization, kaolinization, chloritization, and carbonatization (Figure 3). The silicification is characterized by the formation of hydrothermal quartz within the altered granite. Sericitization and chloritization are widespread throughout the mining district, occurring either as vein-like or disseminated within the granite (Figure 3B,C). These types of alteration are closely associated with high-grade Ag-Au mineralization at the Niujuan deposit.

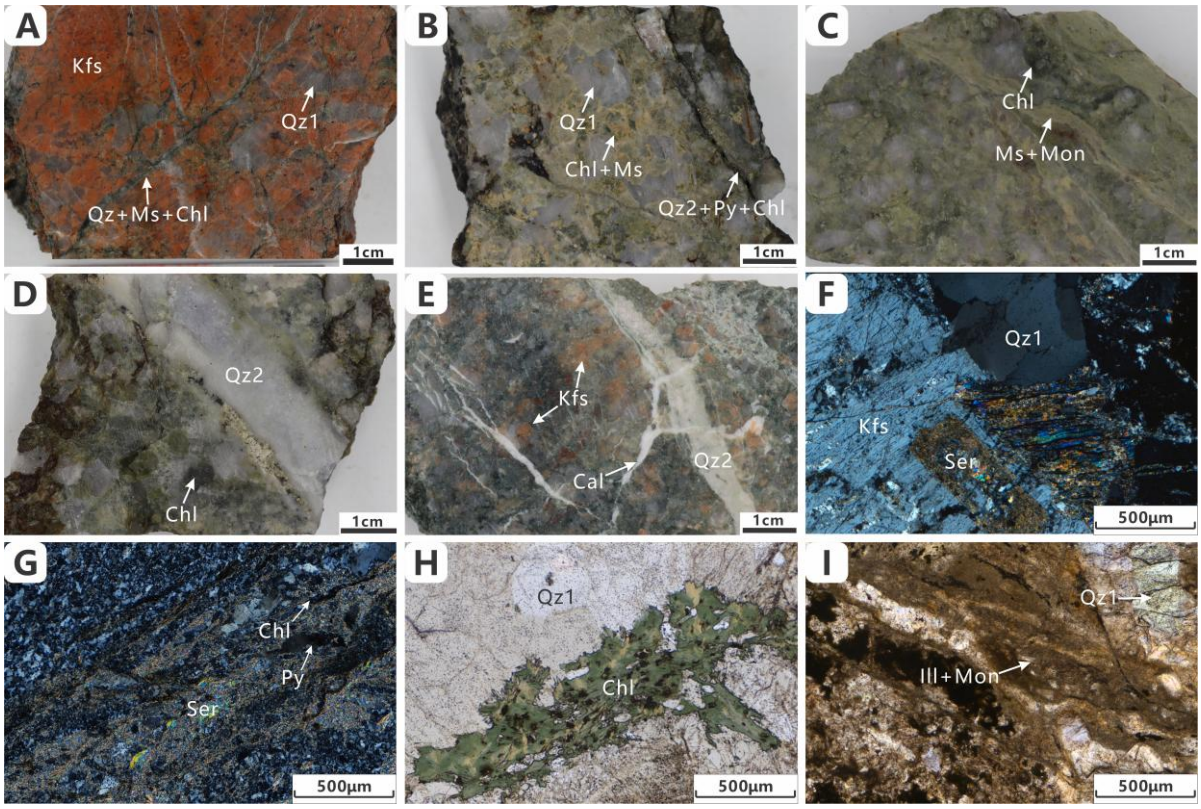

Figure 3. Photographs showing the different alteration types in the Niujuan Ag-Au deposit. (**A**) Strongly K-feldspar-altered granite cut by late-stage quartz-muscovite-chlorite veins. (**B**) Disseminated chloritization and sericitization. (**C**) Silicified granite cut by late-stage illite-montmorillonite vein bodies. (**D**) Quartz vein cutting early-stage chloritized silicified granite. (**E**) Late-stage calcite veinlet cutting quartz veinlet. (**F**) Sericitization of granite (crossed transmitted light). (**G**) Quartz-sericite-chlorite-pyrite veinlets in silicified granite (crossed polarized light). (**H**) Chlorite vein in granite (plane-polarized transmitted light). (**I**) Illite-montmorillonite in silicified granite (plane-polarized transmitted light). Abbreviations: Cal = calcite; Chl = chlorite; Ill = illite; Kfs = k-feldspar; Mon = montmorillonite; Ms = muscovite; Qz = quartz; Py = pyrite.

The ore minerals primarily include galena, sphalerite, pyrite, and chalcopyrite, with minor amounts of arsenopyrite, siderite, and electrum (Figure 4H,I). The valid gangue minerals are dominated by quartz, carbonates, and fluorite.

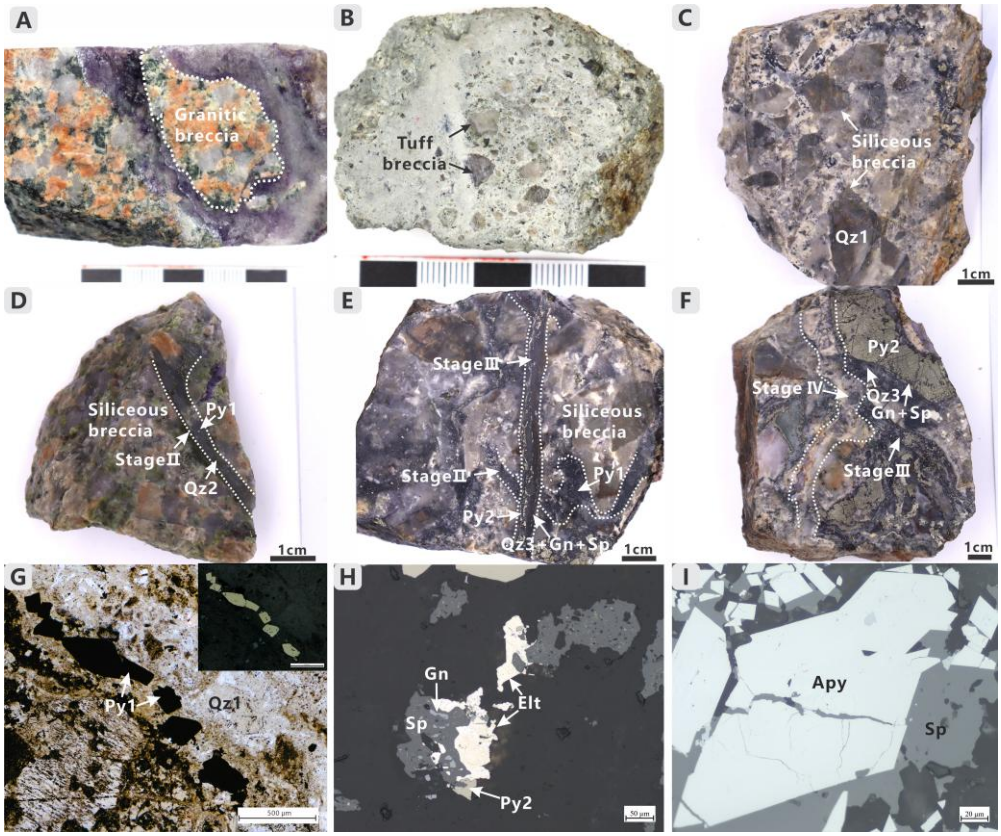

Figure 4. Photographs of typical ores and of the Niujuan Ag-Au deposit. (**A**) Granite breccia hosted by fluorite veins. (**B**) Tuffaceous breccia. (**C**) Siliceous breccia. (**D**) Siliceous breccia cut by an quartz-pyrite veinlet. (**E**) Quartz-pyrite veinlet within siliceous breccia ore, and then cut by polymetallic sulfide veins. (**F**) Polymetallic sulfide veins cut by late fluorite vein. (**G**) Pyrite grains in quartz veins (polarized light). (**H**) Sphalerite, galena, and pyrite assemblages (reflected light). (**I**) Sphalerite coexisting with sub-euhedral arsenopyrite (reflected light). Abbreviations: Apy = arsenopyrite; Elt = electrum; Gn = galena; Qz = quartz; Py = pyrite; Sp = sphalerite.

3. Sampling and Analytical Methods

3.1. Sample Characteristics

Samples from different stages and representative ores from the Niujuan deposit were collected and analyzed. Detailed sample information is shown in Table 1.

Table 1. Characteristics of analyzed samples from the Niujuan deposit.

Sample	Elevation	Sample Details
7609-690.2	+555 m	Galena-pyrite veins
7610-695.6	+549 m	Galena-sphalerite-pyrite veins
7611-780.65	+441 m	Colloidal sphalerite within green fluorite
7613-572.1	+683 m	Galena-pyrite vein cutting through quartz-pyrite vein
7614-1066	+1066 m	Quartz-pyrite stockworks
NJ1-4	+1065 m	Banded siliceous veins
NJ2-4	+1065 m	Breccia type ore
NJ2-6	+1065 m	Galena-pyrite veins cutting through granite breccia
NJ6-14	+1150 m	Polymetallic sulfide veins cutting siliceous breccia
N6-21	+1150 m	Electrum-bearing ore
NJ6-13	+1150 m	Disseminated pyrite-bearing ore
ZK74-8-966.8	+233 m	Quartz-galena-pyrite vein-type ore
QZ604851-77.06	+982 m	Quartz-galena-sphalerite vein-type ore

3.2. Analytical Methods

High-gamma micrography was employed to conduct a detailed structural analysis of pyrite under reflected light using a Zeiss Axioscope 5 microscope (Carl Zeiss AG, Beijing, China). In this study, a fixed γ parameter of 10 and a magnification of 50× were adopted for mineral observation, and the green channel was selected as the primary color for displaying γ-enhanced images.

The BSE analyses of pyrite was conducted in the TIMA laboratory of the Key Laboratory for Exploration Theory and Technology of Critical Mineral Resources, China University of Geosciences, Beijing. The analytical instrument used was the automatic mineral analysis system (TIMA-GMS) (TESCAN, Beijing, China). Prior to the commencement of the analysis, the sample was prepared with a carbon coating process. The BSE analysis conditions were set under vacuum mode, employing a working voltage of 20 keV and a working distance of 15 mm.

Laser ablation–inductively coupled plasma mass spectrometry (LA-ICP-MS) in situ trace element analysis for pyrite was completed at Guangzhou Tuoyan Testing Technology Co., Ltd. (Guangzhou, China). The laboratory employed a New Wave Research 193 nm ArF excimer laser ablation system coupled with a Thermo Scientific iCap-RQ quadrupole inductively coupled plasma mass spectrometer (ICP-MS) (Guangzhou, China). The laser spot diameter was 30 μm, operating at a frequency of 6 Hz and an energy density of 3.5 J/cm^2. During micro-area in situ trace element testing and processing, multi-external standard calibration without internal standards was performed using glass reference materials NIST SRM 610 and MASS-1 [41]. Reference materials SRM 612 and GZTY served as monitoring samples. Analysis of each test point included approximately 40 s of blank signal and 45 s of sample signal. Offline data processing was completed using Iolite software version 4.

Laser ablation multi-collector inductively coupled plasma mass spectrometry (LA-MC-ICP-MS) in situ sulfur isotope analysis of pyrite was performed at Guangzhou Tuoyan Testing Technology Co., Ltd. The laser ablation system was Resolution S155, and the MC-ICP-MS was Neptune Plus (Thermo Fisher Scientific, Guangzhou, China). Helium was used as the carrier gas for the laser ablation system. Analysis employed single-spot mode with a beam spot size of 32 μm, frequency of 4 Hz, and energy density of 5.0 J/cm^2. The Neptune Plus mass spectrometer was equipped with nine Faraday cups and a 1011-ohm resistive amplifier. Operating in medium resolution mode (approximately 7000), it eliminated interference peaks. Three Faraday cups (L3, C, and H3) simultaneously received static signals for 32S, 33S, and 34S, respectively. Sulfur isotope mass fractionation was corrected using the SSB method. The pyrite reference material Balmat [42] was used for pyrite samples.

Hydrogen and oxygen isotope analyses of quartz were performed at Guangzhou Tuoyan Testing Technology Co., Ltd. Prior to analysis, representative quartz samples were selected and ground to a particle size of 200 mesh. For oxygen isotope measurements, the conventional BrF_5 method was employed [43]. Oxygen isotopes were measured using a 253 Plus Gas Isotope Ration Mass Spectrometer (Thermo Fisher Scientific, Guangzhou, China), with an analytical precision of ±0.2‰ relative to the Vienna Standard Mean Ocean Water (V-SMOW). Hydrogen isotopes were analyzed on a MAT-253 mass spectrometer (Guangzhou, China); results were normalized to the IAEA-VSMOW standard and yielded an analytical precision of 2.0‰.

4. Results

4.1. Mineralization Stages

Based on cross-cutting relationships and hydrothermal mineral assemblages (Figure 5), the Niujuan deposit reveals a paragenetic sequence consisting of four distinct stages of mineralization.

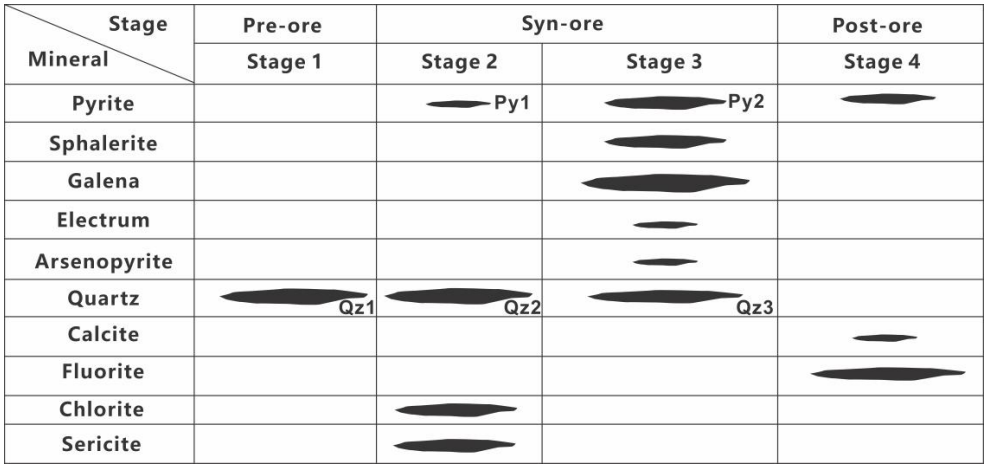

Figure 5. Paragenetic sequence of minerals from the Niujuan Ag-Au deposit.

(1) Pre-ore siliceous breccia stage (stage 1): This stage is characterized by the formation of hydrothermal breccia that was cemented by fine-grained quartz. Much breccia is developed and can be classified into three types based on its composition: granitic breccia (Figure 4A), tuffaceous breccia (Figure 4B), and siliceous breccia (Figure 4C).

(2) Syn-ore quartz-pyrite stage (stage 2): The quartz vein/veinlets occurring as smoky gray in color cut through early siliceous rocks (Figure 4D), with widths ranging from 0.1 to 3 cm. The mineral composition is relatively simple; only quartz and minor pyrite (Py1) were identified. Py1 occurs mainly as fine-grained euhedral or sub-euhedral grains (Figure 4G). Chlorite and sericite occur in the veins during this stage (Figure 3G,H).

(3) Syn-ore polymetallic sulfide stage (stage 3): This represents the main mineralization stage. Except for quartz, abundant sulfides precipitated, including galena, sphalerite, pyrite, chalcopyrite, and arsenopyrite. Fine-grained electrum was commonly hosted within pyrite (Figure 4E,F).

(4) Post-ore fluorite-calcite stage (stage 4): This stage is characterized by the development of fluorite with different colors. These veins, approximately 1–2 cm wide, consist primarily of fluorite with minor calcite (Figure 4F).

4.2. Microscopic Texture Characteristics of Pyrite

This study combined both the gamma-enhanced reflected light imaging and scanning electron microscopy backscattered electron (BSE) imaging techniques to reveal the textures of pyrite. The brightness differences between these two methods reflect varying arsenic (As) concentrations within the pyrite [44]. The results indicate that pyrite from the quartz-pyrite stage (Py1) is euhedral, medium- to fine-grained, and texturally homogeneous. It is characterized by numerous pores, some of which are infilled with galena and sphalerite (Figure 6A). Pyrite from the polymetallic sulfide stage (Py2) shows core-mantle-rim textures; the core, mantle, and rim are designated Py2a, Py2b, and Py2c, respectively. Py2 is typically featured with numerous galena and sphalerite inclusions. Py2a typically exhibits a porous texture. Py2b appears relatively dark in gamma images but brighter in corresponding BSE images (Figure 6B,C), reflecting a higher arsenic content than the core. Py2c either

overgrows earlier pyrite (Py2a and Py2b) (Figure 6B–F) or occurs as isolate grains. Electrum grains are hosted as fine-grained inclusions within Py2c, or distributed as larger grains close to Py2c (Figure 6G–I).

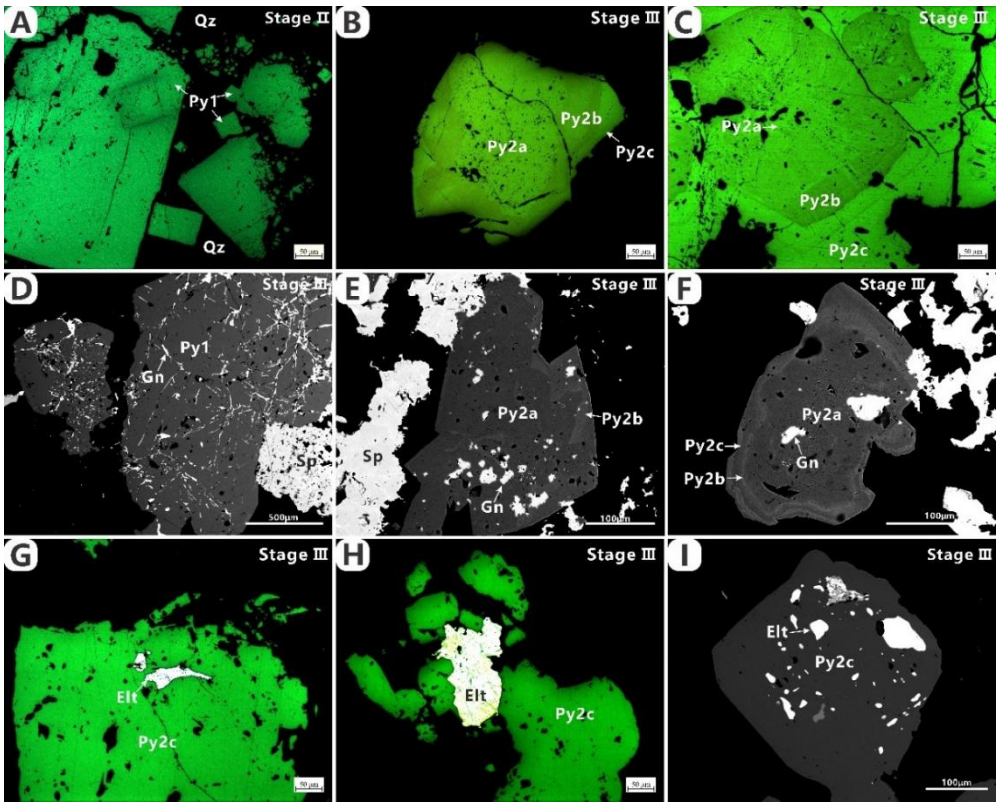

Figure 6. Backscattered electron (BSE) and gamma-enhanced photographs showing the microscopic texture of pyrite of the Niujuan Ag deposit. (**A**) Homogeneous pyrite grains within quartz-pyrite veins. (**B**,**C**) Multi-generational pyrite from the polymetallic sulfide stage, showing core-mantle-rim texture. (**D**) Galena inclusions distributed along Py1 fractures. (**E**,**F**) Different generations of pyrite with different brightness in BSE images. (**G**,**H**) Py2c associated with electrum. (**I**) Small electrum grains within Py2c. Abbreviations: Elt = electrum; Gn = galena; Qz = quartz; Py = pyrite.

4.3. Trace Element Composition

To minimize the influence of mineral inclusions on pyrite trace element compositions, time intervals with relatively stable ablation signals were carefully checked for calculating elemental concentrations. Final data were cross-checked individually, and anomalously high values were removed. The LA-ICP-MS trace element analysis results for pyrite are presented in Table 2. The trace element concentrations for spot analyses below detection limits are shown and reported as zero. Trace element concentrations in pyrite from different stages and generations vary systematically, with the most pronounced variations observed in As, Ag, Sb, Pb, Mn, Co, and Ni. The content of invisible Au in pyrite from different stages was generally less than 7 ppm, showing a positive correlation between Au and As (Figure 7A). Co and Ni did not differ significantly among stages but exhibited a generally positive correlation. Py1 was characterized by relatively low Ag contents, with a maximum of 21.8 ppm and an average of 5.8 ppm. Arsenic in Py1 showed the lowest concentrations, mainly ranging from 2.4 to 136.4 ppm, with a maximum of 136.4 ppm and an average of 45.9 ppm. Py2 was enriched in As and Ag; however, no clear positive correlation between these elements was observed. In Py2a, Ag reached a maximum of 118.4 ppm (average 18.1 ppm), whereas As attained a maximum of 3613.1 ppm (average 713.2 ppm). Sb was also relatively high concentrations: up to 88.4 ppm and with an average of 16.9 ppm. In

Py2b, Sb was mostly below the detection limit, with an average of ~1 ppm, whereas As and Au were relatively enriched, averaging 6670.8 ppm (range: 217.4–25,455.8 ppm) and 1.4 ppm (range: <0.1–7.3 ppm), respectively. Ag showed pronounced variability, with several analyses exceeding 200 ppm, reaching a maximum of 370.3 ppm and an average of 38.1 ppm. Trace element concentrations in Py2c were markedly lower than those in Py2b, with Ag up to 74.4 ppm (average 7.7 ppm) and As reaching a maximum of 3137.6 ppm, commonly associated with Au concentrations <1 ppm.

Table 2. Trace element composition of pyrite from the Niujuan Ag-Au deposit by LA-ICP-MS (10-6).

Sample No.	Type	Mn ppm	Co ppm	Ni ppm	Cu ppm	Zn ppm	As ppm	Ag ppm	Sb ppm	Au ppm	Pb ppm
7609-646.1-24	Py1	106.5	41.1	10.1	3.1	0.4	47.3	5.5	2.1	0.0	17.0
7610-692.4-8	Py1	50.8	0.1	0.2	2.7	2.5	11.7	21.8	6.9	0.0	71.0
7610-692.4-9	Py1	0.6	60.7	4.6	0.1	0.4	28.2	0.1	0.1	0.0	1.1
7611-780.65-7	Py1	61.4	201.6	4.6	309.5	23.4	136.4	8.9	1.4	0.0	163.2
7613-590.8-13	Py1	13.6	7.0	2.4	0.4	2.1	52.2	0.2	0.3	0.0	6.0
7613-572.1-2	Py1	6.4	56.0	1.3	3.4	1.2	10.9	2.3	1.9	0.0	56.5
7613-572.1-3	Py1	9.5	6.0	0.8	218.0	9.4	98.1	17.1	12.9	0.0	355.4
7614-1066-7	Py1	0.3	14.9	0.5	0.2	0.6	66.6	0.0	0.0	0.0	9.0
7614-1066-8	Py1	3.1	2.1	0.2	0.8	0.4	5.1	0.1	0.1	0.0	18.0
7614-1066-9	Py1	1.9	1.5	0.1	0.9	0.9	2.4	0.4	0.0	0.0	2.8
7614-1063-10	Py1	0.1	6.6	0.6	4.1	1.2	46.3	7.6	0.1	0.0	24.3
7609-377.2-18	Py2a	0.2	0.5	5.9	2.6	0.4	291.4	50.2	0.5	0.2	19.2
7609-377.2-19	Py2a	8.4	7.4	7.6	29.2	1.2	67.0	118.4	1.3	0.2	45.7
7609-673.3-6	Py2a	0.1	0.0	0.0	1.1	0.0	332.9	0.5	3.9	0.0	43.6
7609-673.3-7	Py2a	1.1	3.9	0.5	36.4	11.8	114.5	22.7	62.8	0.1	329.1
7611-832.55-1	Py2a	0.2	15.7	5.9	75.8	4.2	19.8	1.1	0.1	0.0	12.5
7611-832.55-3	Py2a	52.7	94.2	26.2	54.7	15.5	791.8	11.4	78.5	0.2	785.4
NJ6-28-10	Py2a	5.3	0.9	0.0	1.4	54.0	1553.3	7.6	1.0	0.0	24.9
NJ6-28-13	Py2a	0.2	0.0	0.1	1.2	0.6	233.7	10.1	2.5	0.0	15.4
NJ2-4-14	Py2a	0.2	1.3	0.1	0.4	0.4	110.2	0.8	0.3	0.1	18.1
NJ2-6-51-10	Py2a	458.7	18.4	4.2	5.3	1.6	1997.1	8.6	3.5	0.3	57.3
NJ4-1-54-13	Py2a	0.2	0.0	0.0	4.3	0.2	255.9	25.8	13.8	0.0	101.8
NJ6-21-2	Py2a	0.1	0.0	0.0	0.1	0.2	314.5	0.4	0.0	0.0	0.0
7609.662.7-1	Py2a	285.3	0.1	0.0	39.1	0.6	66.9	24.2	60.8	0.0	179.0
7610-695.5-2	Py2a	1.0	0.0	0.0	6.5	0.4	0.8	13.7	13.1	0.0	160.8
7611-708.45-10	Py2a	1.2	0.8	39.8	1.3	1522.9	416.4	32.8	2.1	0.0	267.5
7611-708.45-11	Py2a	3.4	2.0	110.0	0.7	2683.2	4.3	3.3	2.1	0.0	109.4
7609-646.1-26	Py2a	53.2	0.2	0.4	1.3	231.9	2272.4	3.9	0.6	0.2	3.8
7609.662.7-2	Py2a	185.7	52.2	4.3	41.0	0.8	654.3	19.1	88.4	0.0	170.0
7609.662.7-3	Py2a	62.1	1.7	0.1	1.0	0.7	1154.1	0.8	0.4	0.4	9.7
NJ2-6-51-8	Py2a	419.2	17.3	0.4	5.3	2.9	3613.1	5.7	2.8	0.4	368.5
7609-377.2-17	Py2b	0.3	18.3	1.2	45.1	0.5	6176.1	25.0	6.9	0.6	138.4
7609-646.1-25	Py2b	43.6	0.1	0.2	0.7	1.4	2045.0	15.7	0.7	0.1	131.6
7609-646.1-27	Py2b	9.5	0.1	0.0	0.3	0.1	1851.8	0.4	0.2	0.1	1.8
7609-690.4-5	Py2b	0.2	207.9	4.0	0.4	0.0	217.4	0.9	0.9	0.0	441.4
7610-675.2-7	Py2b	0.3	382.4	39.2	0.5	27.0	1165.6	33.5	0.1	0.0	0.6
7610-675.2-8	Py2b	97.2	115.5	40.1	6.4	0.1	1577.0	370.3	11.5	0.3	34.5
7611-780.65-8	Py2b	0.1	41.1	8.9	9.5	0.3	7043.5	1.0	2.8	3.4	25.1
NJ1-4-49-13	Py2b	0.3	2.4	0.4	8.7	4.2	8410.8	2.6	0.5	1.6	7.6
NJ1-4-49-14	Py2b	0.2	1.0	0.2	27.3	0.3	14,686.8	1.8	0.5	5.4	8.8
NJ1-4-49-15	Py2b	0.2	2.7	0.5	16.9	0.1	10,358.1	4.1	0.8	4.2	11.2
NJ1-4-49-16	Py2b	0.1	8.5	1.7	13.0	0.4	25,455.8	3.1	1.8	7.3	7.0
NJ1-4-49-17	Py2b	13.2	5.1	2.3	4.6	414.1	2937.8	10.3	6.0	0.8	219.0
NJ2-6-51-9	Py2b	17.4	12.4	0.8	12.0	3.2	13,805.1	1.6	1.6	5.2	14.7
NJ2-8-1	Py2b	11.4	2.6	0.2	11.4	6.3	7817.6	0.9	0.5	1.7	10.1
NJ2-8-5	Py2b	4.0	3.6	0.6	5.7	0.4	7481.3	1.2	0.2	1.0	33.4
NJ6-28-11	Py2b	0.1	0.2	0.1	1.2	0.4	5039.6	0.1	0.0	0.2	0.0
NJ6-28-12	Py2b	0.7	0.0	0.0	1.2	5.2	3326.9	12.5	1.9	0.1	2.7

Table 2. *Cont.*

Sample No.	Type	Mn ppm	Co ppm	Ni ppm	Cu ppm	Zn ppm	As ppm	Ag ppm	Sb ppm	Au ppm	Pb ppm
NJ2-4-15	Py2b	0.1	18.4	6.4	16.1	0.4	11,944.7	0.3	0.0	3.6	0.4
NJ4-4-56-2	Py2b	0.1	3.9	0.0	3.7	0.0	10,223.5	0.1	0.0	0.7	0.2
NJ4-4-56-3	Py2b	0.2	2.3	0.6	7.2	4.2	6418.8	274.0	0.1	0.8	3.2
NJ4-4-56-4	Py2b	0.4	8.4	0.3	7.0	18.6	2186.9	309.5	0.0	0.4	2.6
NJ4-1-54-11	Py2b	0.2	0.1	0.1	5.6	0.5	8692.2	1.7	0.1	1.6	7.6
NJ6-21-1	Py2b	2.0	0.5	0.1	5.0	0.2	5338.1	4.1	0.3	1.1	1.9
7609-377.2-22	Py2b	2.7	434.2	6.4	55.0	19.0	5258.3	29.2	4.9	0.5	44.6
NJ4-8-58-6	Py2b	0.1	4.6	0.0	1.7	0.5	8770.4	0.0	0.0	0.8	0.1
NJ4-8-58-7	Py2b	0.0	0.1	0.0	1.4	0.0	6360.6	0.0	0.0	0.2	0.0
NJ4-8-58-8	Py2b	0.0	0.0	0.1	0.7	0.2	2186.3	0.0	0.0	0.0	0.0
NJ4-8-58-9	Py2b	0.0	0.1	0.0	0.5	0.5	4555.6	0.0	0.0	0.1	0.0
NJ2-8-2	Py2b	0.2	0.0	0.0	0.1	0.4	2120.6	0.3	0.0	0.0	0.3
NJ1-4-49-12	Py2c	2.1	23.8	5.4	7.5	0.5	2166.3	1.0	0.1	0.3	11.5
NJ1-4-49-18	Py2c	51.7	44.2	3.2	6.1	16.5	801.2	6.7	58.1	0.0	488.6
NJ6-14-66-5	Py2c	2.5	0.5	0.0	0.3	0.5	1675.4	0.2	0.1	0.0	1.0
NJ6-14-66-6	Py2c	2.5	152.5	2.0	4.5	17.3	370.3	74.4	0.9	0.1	39.8
NJ6-14-66-7	Py2c	0.3	58.8	1.4	2.9	0.7	2906.6	5.5	1.0	0.1	8.3
NJ2-8-3	Py2c	0.4	0.6	0.0	1.1	3.7	2404.7	0.1	0.0	0.1	0.6
NJ2-8-4	Py2c	131.4	0.0	0.0	0.5	0.3	1230.3	0.9	0.2	0.0	3.1
NJ4-1-54-12	Py2c	0.0	7.0	1.4	1.0	0.0	1724.0	0.5	0.0	0.3	0.8
7611-780.65-9	Py2c	0.3	0.1	0.0	0.2	0.3	3137.6	0.0	0.0	0.0	0.0
7611-780.65-10	Py2c	0.2	14.3	3.0	3.4	0.4	2306.0	1.2	5.3	0.4	62.6
7610-730.4-5	Py2c	5.6	3.1	3.9	211.8	205.7	1399.4	6.4	11.8	0.8	99.2
7613-572.1-4	Py2c	28.8	5.4	1.5	15.9	1.6	1961.7	3.2	5.8	0.5	590.1
7613-572.1-5	Py2c	39.8	255.2	9.9	5.2	0.5	2171.2	1.7	1.2	0.5	17.0
7613-572.1-6	Py2c	10.3	2.8	6.7	70.0	5.7	1095.0	5.3	5.3	0.1	322.8

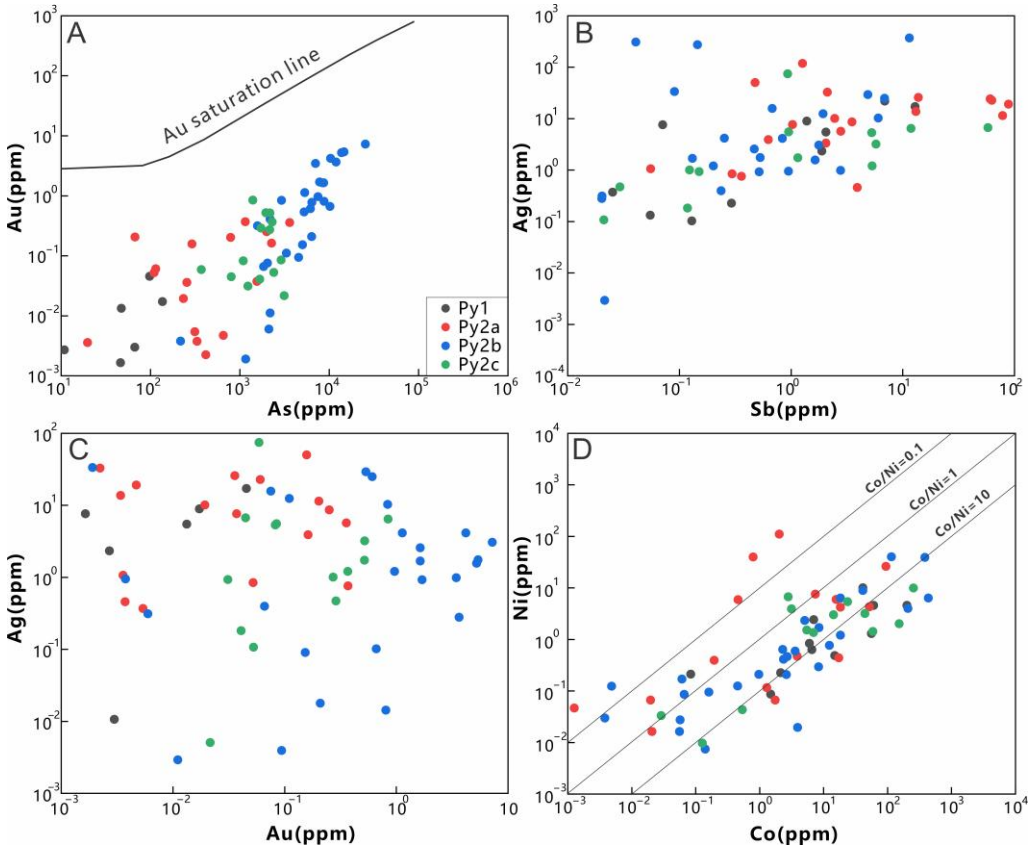

Figure 7. Diagrams showing the trace element relationships of pyrite of the Niujuan Ag-Au deposit. (**A**) Au-As; (**B**) Ag-Sb; (**C**) Ag-Au; (**D**) Ni-Co.

4.4. Sulfur Isotope Composition

The $\delta^{34}S$ values of pyrite from the Niujuan Ag-Au deposit are shown in Figure 8 and Table 3. Pyrite from different stages displays relatively uniform $\delta^{34}S$ values, mainly between 3.8‰ and 6.7‰. The $\delta^{34}S$ values of Py1 range from 3.8‰ to 6.7‰, with an average of 4.9‰, whereas those of Py2 range from 4.3‰ to 6.6‰, averaging 5.3‰.

Table 3. Sulfur isotope compositions of pyrite at Niujuan and several Jiaodong-type gold deposits.

Deposit	Sample	Mineral	$\delta^{34}S$	Data Soure	Deposit	Sample	Mineral	$\delta^{34}S$	Data Soure
Niujuan	7609-646.1-1	Py1	3.8		Jiaodong	20XC02-2	pyrite	5.2	[15]
	7609-646.1-2	Py1	4.1			20XC02-3	pyrite	5.1	
	7610-695.6-1	Py1	5.9			20XC02-4	pyrite	5.4	
	7610-695.6-2	Py1	3.9			20XC02-4	pyrite	5.4	
	7613-590.8-1	Py1	4.1			20XC02-5	pyrite	5.0	
	7613-590.8-2	Py1	4.9			20QJ34-20	pyrite	7.0	
	7614-1066-1	Py1	6.1			20QJ34-21	pyrite	6.4	
	7614-1066-2	Py1	6.7			20QJ34-22	pyrite	5.2	
	NJ2-4-1	Py2a	5.1			C800-6/2	pyrite	5.1	[45]
	NJ1-4-1	Py2b	6.4			C800-6/3	pyrite	5.2	
	NJ1-4-2	Py2b	5.1			LK10	pyrite	9.7	[46]
	NJ1-4-3	Py2b	5.5			LK12	pyrite	9.5	
	NJ2-4-4	Py2b	6.0			LK14	pyrite	9.3	
	NJ4-4-1	Py2b	5.2			LK15	pyrite	9.7	
	NJ4-4-2	Py2b	5.0			TK1	pyrrhotite	9.7	
	7609-646.1-1	Py2c	6.0			TK4	pyrrhotite	10.6	
	7609-646.1-2	Py2c	4.7			K2	pyrite	8.5	
	7609-646.1-3	Py2c	5.8			K3	pyrite	9.1	
	7609-673.3-1	Py2c	4.3			141	pyrite	10.7	[47]
	7609-673.3-2	Py2c	5.0			432	pyrite	11.7	
	7611-708.45-1	Py2c	6.2			494	pyrite	11.3	
	7611-708.45-2	Py2c	6.6			102	pyrite	8.5	
	7611-780.65-1	Py2c	4.8			111	pyrite	8.7	
	7611-780.65-2	Py2c	5.0			431	pyrite	10.6	
	7611-780.65-3	Py2c	5.0			517	pyrite	8.8	
	NJ1-4-4	Py2c	5.4			782	pyrite	11.0	
	NJ1-4-5	Py2c	5.3			501	pyrite	10.3	
	NJ6-14-1	Py2c	4.7			503	pyrite	11.8	
	NJ6-14-2	Py2c	5.2			505	pyrite	10.5	
	NJ-11	Pyrite	4.2	[26]		506	pyrite	11.2	
	NJ-69	Pyrite	5.7			TW-1	pyrite	11.2	[48]
	NJ-71-1	Pyrite	5.6			TW-2	pyrite	10.5	
	NJ-72	Pyrite	4.4			X-11	Galena	9.1	
	NJ-73	Pyrite	4.0			DZ-013	pyrite	10.5	
	NJ-71-2	Galena	2.5			DZ-015	pyrite	11.5	
	NJ-74	Galena	3.1			15JT-10-1	pyrite	5.5	[49]
	5-73-5	Galena	2.4	[27]		15JT-07-1	pyrite	5.7	
	5-73-5	Sphalerite	5.2			15JT07-2	pyrite	5.6	
	5-73-4	Sphalerite	5.3			15JT-O5	pyrite	6.1	
	5-73-4	Galena	3.1			15JT-21	pyrite	5.9	
	1-73-5	Pyrite	2.6			15JT-25	pyrite	6.0	
	1-77-6	Pyrite	3.6			15JT-27	pyrite	5.5	
	5-71-3	Pyrite	4.7						

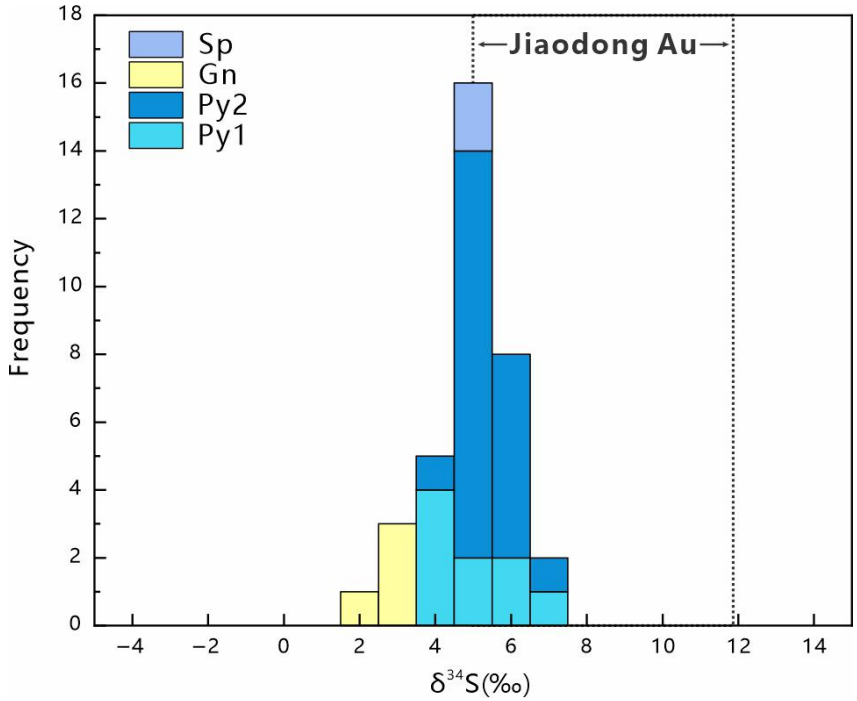

Figure 8. Distribution histogram of sulfides $\delta^{34}S$ isotope composition in the Niujuan deposit.

4.5. Hydrogen and Oxygen Isotope Composition

Hydrogen and oxygen isotope data are listed in Table 4. Quartz $\delta^{18}O_{V\text{-}SMOW}$ values ranged from 1.5 to 3.8‰ and showed only minor variations among stages. Similarly, δD values displayed a narrow range from −119.5 to −103.5‰. All data were plotted within the mixing field between magmatic and meteoric waters.

Table 4. Hydrogen and oxygen isotope compositions of quartz and equilibrated fluid at Niujuan and several Jiaodong-type gold deposits.

Deposit	Mineral	Stage	$d^{18}O_{V\text{-}SMOW}$‰	T (°C)	$d^{18}O_{fluid}$ (‰)	δD_{fluid} (‰)	Data Soure
Niujuan	Quartz	II	2.7	270	−5.3	−119.5	This Study
	Quartz	III	3.3	250	−5.7	−109.8	
	Quartz	III	1.5	250	−7.5	−111.5	
	Quartz		5.3		−2.8	-	[26]
	Quartz		4.0		−4.1	−125.8	
	Quartz		1.5		−6.6	−130.8	
	Quartz		4.1		−4.0	−122.8	
	Quartz		1.1		−7.0	−128.3	
	Quartz		3.0		−3.9	−119.4	[27]
	Quartz		2.5		−5.6	−113.2	
	Quartz		0.6		−7.5	−104.3	
Jiaodong	Quartz		10.2		7.8	−63.8	[18]
	Quartz		13.0		10.9	−67.8	
	Quartz		13.4		10.9	−67.4	
	Quartz		13.7		8.5	−77.2	
	Quartz		13.4		7.5	−79.1	
	Quartz		13.2		7.7	−66.4	
	Quartz		12.8		7.7	−70.4	
	Quartz		13.1		7.0	−80.6	

Table 4. *Cont.*

Deposit	Mineral	Stage	$d^{18}O_{V\text{-}SMOW}$‰	T (°C)	$d^{18}O_{fluid}$ (‰)	δD_{fluid} (‰)	Data Soure
Jiaodong	Quartz		12.3		7.8	−94.0	[50]
	Quartz		12.0		8.0	−90.0	
	Quartz		13.0		8.9	−96.0	
	Quartz		12.9		9.6	−91.0	
	Quartz		13.1		9.9	−92.0	
	Quartz		12.4		9.9	−99.0	
	Quartz		12.1		3.3	−67.2	
	Quartz		14.4		5.6	−73.0	
	Quartz		13.7		4.9	−75.2	
	Quartz		15.3		6.5	−68.9	
	Quartz		13.7		4.9	−71.7	
	Quartz		16.7		0.5	−70.1	
	Quartz		13.8		5.0	−74.1	
	Quartz		14.4		5.6	−92.7	
	Quartz		15.2		6.4	−81.8	
	Quartz		13.9		5.1	−86.0	
	Quartz		15.7		6.9	−95.7	
	Quartz		14.8		7.1	−82.7	[51]
	Quartz		15.2		7.5	−83.6	
	Quartz		15.9		7.3	−87.6	
	Quartz		14.8		5.9	−80.7	
	Quartz		15.6		6.5	−83.9	
	Quartz		14.1		7.4	−83.5	[52]
	Quartz		13.1		6.4	−75.2	
	Quartz		14.1		7.8	−85.2	
	Quartz		13.8		7.7	−75.2	
	Quartz		13.0		6.0	−82.5	
	Quartz		15.0		6.9	−68.7	
	Quartz		15.8		8.4	−73.2	

Note: The temperatures are based on unpublished fluid inclusion thermometry data.

5. Discussion

5.1. Characteristics of Trace Element Composition in Pyrite

Pyrite is one of the most common sulfides in the Earth's crust, and its trace element composition plays a crucial role in tracing fluid evolution and mineralization processes [11,52–55]. Determining the occurrence of trace elements, whether as lattice-bound components, nanoparticles, or micro-inclusions, is therefore a prerequisite for interpreting their geochemical behavior in pyrite [56–60].

As shown in Figure 9, laser ablation signals for most trace elements in pyrite are predominantly flat and stable, suggesting that these elements are mainly incorporated into the pyrite lattice or occur as nanoparticles [61]. In contrast, anomalous signal spikes of Pb, Zn, and Ag observed in some analyses indicate the presence of micrometer-scale inclusions of Pb- and Zn-rich minerals, such as galena and sphalerite. This is supported by the common occurrence of galena and sphalerite within the fracture or inclusions within pyrite (Figure 6D–F).

Cobalt and Ni commonly substitute for Fe in the pyrite lattice as Co^{2+} and Ni^{2+}, and the Co/Ni ratio has been used as an indicator of pyrite formation environment. Based on traditional electron microprobe datasets, volcanic-related pyrite typically shows Co/Ni ratios of 5–50, magmatic-hydrothermal pyrite ranges from 1 to 5, and sedimentary pyrite generally exhibits ratios < 1 [62–64]. At Niujuan, pyrite from different stages displays a wide range of Co/Ni ratios (0.02–201.21). These pyrites occur exclusively within quartz veins, with its Co/Ni ratio gradually decreasing from approximately 1 to 0.5, indicating that these pyrites are predominantly of magmatic-hydrothermal origin. The availability of increasing

LA-ICP-MS trace element datasets further confirms this limitation. For example, Cao [65] compiled trace element data from 4092 pyrite analyses across 67 orogenic gold deposits worldwide and reported Co/Ni ratios spanning more than four orders of magnitude (>100 to <0.01).

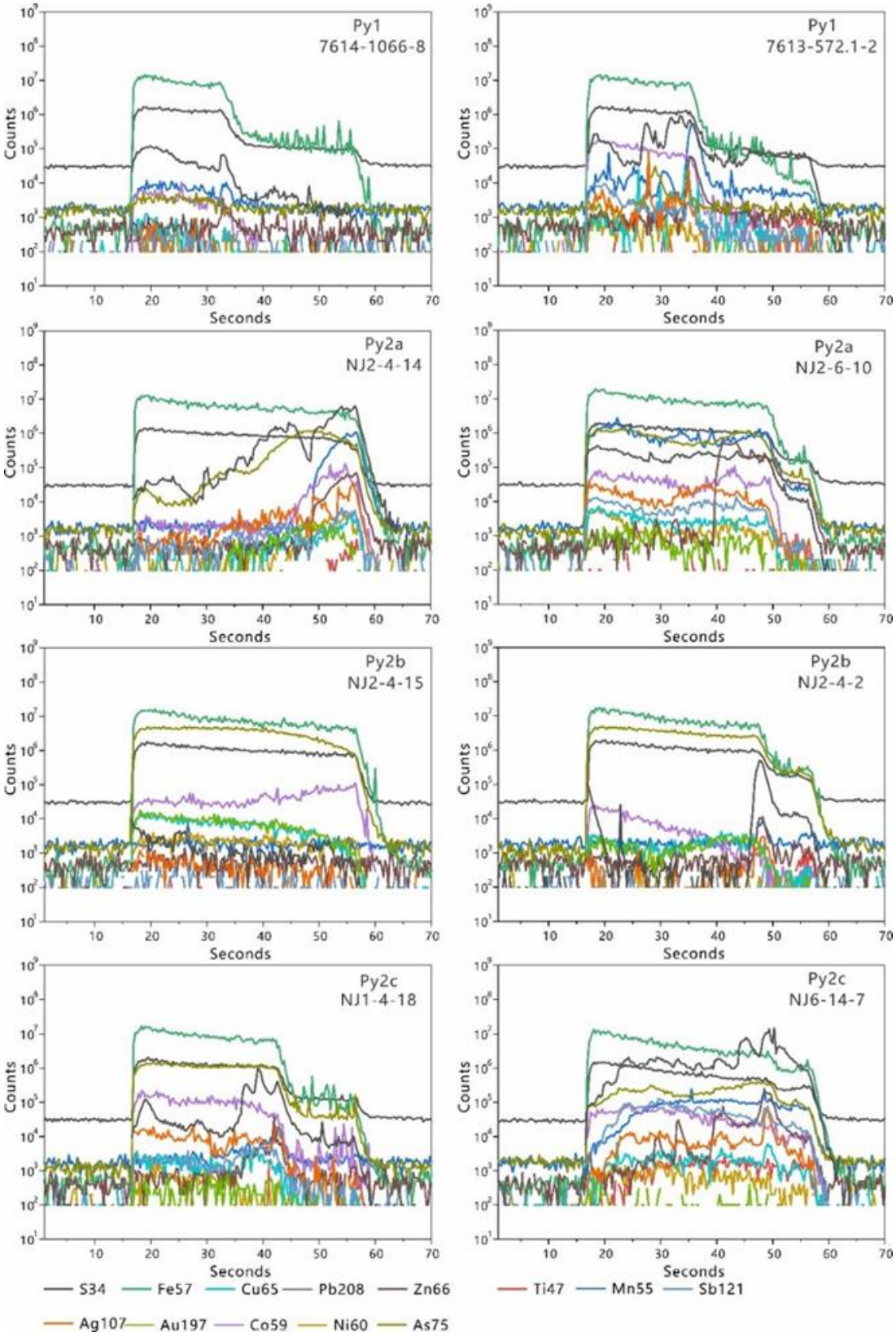

Figure 9. Representative time-resolved LA-ICP-MS depth profiles for the pyrite in the Niujuan deposit.

The well-developed textural zoning of pyrite from different stages at Niujuan provides an opportunity to use trace element variations to constrain the ore-forming process. Concentrations of Au, Ag, and As in Py1 are generally lower than those in Py2, indicating that Au and Ag enrichment reached its highest levels during the main mineralization stage. This enrichment provided favorable conditions for the precipitation of abundant electrum. A positive correlation between As and Au concentrations in pyrite, with data plotting below the Au solubility line (Figure 7A), suggests that invisible gold is dominantly present as lattice-bound Au [56]. Extensive studies have shown that during relatively slow crystal growth, As incorporation reduces pyrite lattice symmetry and enhances Au uptake [66,67], whereas rapid, non-equilibrium growth may result in decoupling between micrometer-scale Au and As [68]. A positive correlation between As and Au was observed in this study (Figure 7A), implying that As plays a key role in controlling Au enrichment at the deposit scale.

Py2b contains the highest Au and As concentrations among all pyrite stages/generations; however, Au contents remain relatively low, with a maximum of 7.3 ppm and an average of 1.4 ppm, whereas As ranges from 217.4 to 25,455.8 ppm, with an average of 6670.8 ppm. Similarly, invisible Au contents in pyrite from Au deposits in Jiaodong Province, the NCC, commonly contain <1 ppm, comparable to those at Niujuan [10,65]. The low invisible gold content is significantly lower than that of Carlin-type gold deposits. For example, pyrite from the main mineralization stage of the Shuiyindong Au deposit, Youjiang Basin, South China, contains up to 641 ppm invisible Au and 9147 ppm As [69]. Au contents are also lower than those reported for some vein-type gold deposits in the Jiangnan Orogenic Belt, such as the Gutaishan deposit, where pyrite from the main mineralization stage contains up to 51 ppm Au [61]. These contrasts reflect not only differences in deposit types but also variations in Au precipitation mechanisms. Carlin-type deposits are characterized by disseminated mineralization and typically lack native gold [69,70], whereas pyrite from both vein-type and disseminated ores in Jiaodong Province commonly hosts native gold and electrum [13,16].

5.2. Sources of Metals and Fluids

The development of in situ analytical techniques with small beam size and low detection limits has greatly improved our understanding of mineralization processes (e.g., [54,71,72]). The occurrence of overgrowth textures in pyrite commonly indicates the involvement of multiple sulfur sources. For example, pyrite from Carlin-type gold deposits typically displays sedimentary cores overgrown by hydrothermal rims, with pyrite of different origins distinguished by contrasting sulfur isotopic compositions [69,73]. For example, sedimentary pyrite displays $\delta^{34}S$ values of +15.6‰ to +25.8‰, which differ markedly from those of hydrothermal pyrite (0 ± 5‰) in the Yuhengtang and Gutaishan gold deposits of the Jiangnan Orogenic Belt, South China [61,74]. Previous studies [54,75,76] conducted in situ LA-ICP-MS trace element and sulfur isotope analyses on six generations of pyrite from the orogenic Sukhoi Log Au deposit. The results showed that sedimentary-stage Py1 contains the highest Au concentrations (0.4–12.1 ppm), whereas Py2–Py6, formed during diagenetic to metamorphic stages, exhibit much lower Au contents (average 0.07–1.02 ppm). Corresponding $\delta^{34}S$ values also vary systematically among generations (Py1 + Py2: −6.5‰ to +19.3‰; Py3: −2.7‰ to +6.7‰; Py4: 4.3‰ to 24‰; Py5: 7.1‰ to 12.6‰), highlighting the utility of combined trace element and sulfur isotope data in discriminating the sources of ore-forming materials.

In the Niujuan deposit, sulfur isotope compositions of pyrite from different stages show a narrow range, and those values are comparable to those of coexisting galena and sphalerite (Figure 8), suggesting sulfur isotopic equilibrium within the hydrother-

mal system. The small ranges of $\delta^{34}S$ values broadly overlap with the typical range of magmatic sulfur (0 ± 5‰) [77,78], indicating a major contribution of magmatic sulfur. Geochronological data indicate that the Niujuan deposit formed during the Yanshanian period (139.2 ± 3.8 Ma) [27], which makes it significantly younger than the host-rock coarse-grained granite (268.7 ± 3.2 Ma and 254.2 ± 2.8 Ma, respectively) [36]. Consequently, the derivation of ore-forming fluids and metals solely from synorogenic metamorphic devolatilization of the wall rocks is unlikely [79]. Instead, the sulfur involved in mineralization is best interpreted as being sourced predominantly from magmatic–hydrothermal fluids [26]. This S isotope signature is overlapping from that of the Jiaodong Au deposit (Figure 8), which has been interpreted to be sourced from concealed magma (e.g., [80]).

Despite the similarity in sulfur isotopic compositions, the sources of ore-forming fluids differ markedly between the Niujuan Ag-Au deposit and the Jiaodong Au deposits (Figure 10). Published H-O isotope data for quartz from the Jiaodong Au deposits indicate a dominantly magmatic fluid source as most data were plotted within the magmatic water field. This interpretation has been linked to extensive coeval magmatism adjacent to the ore deposits. Fluid inclusion studies have further suggested that the Jiaodong Au deposits formed at depths of approximately 5–6 km [81]. In contrast, fluid inclusion data indicate that the Niujuan deposit formed at a shallower depth of approximately 0.42–0.86 km [82]. The widespread occurrence of breccias also supports formation at relatively shallow crustal levels (Figure 4A–C). Fluid inclusion homogenization temperatures from the Niujuan deposit mostly range between 230 °C and 310 °C [83], which makes them broadly comparable but slightly lower compared to those of the Jiaodong Au deposits (200 °C to 300 °C) [81]. Therefore, temperature is unlikely to be the primary factor controlling the observed differences in fluid composition. This inference is further supported by the broadly similar trace element compositions of pyrite from the two deposits (Figure 11C). We thus propose that differences in formation depth played a critical role in controlling the contrasting metal precipitation.

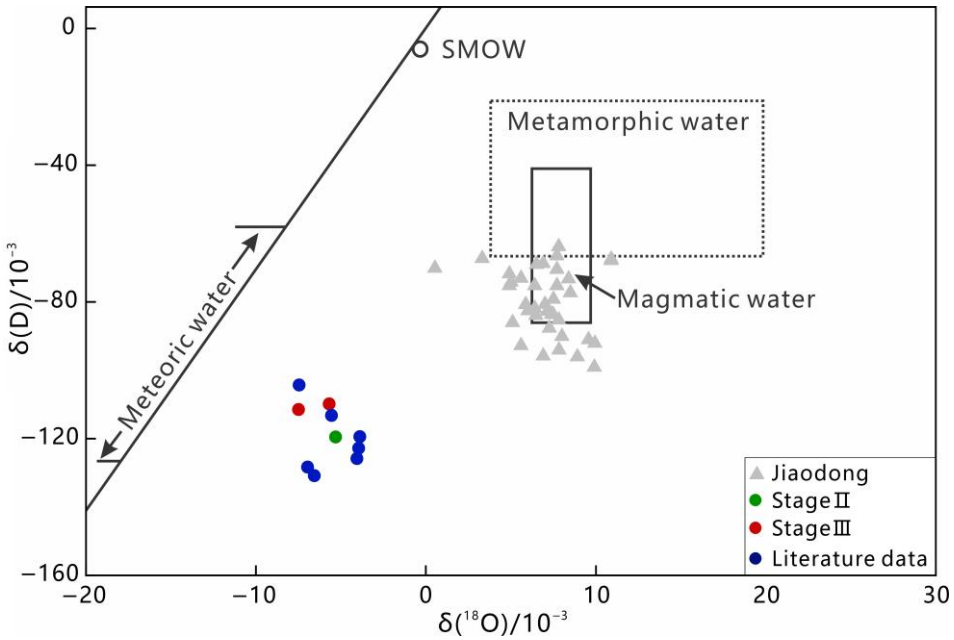

Figure 10. Hydrogen and oxygen isotopic composition of the Niujuan Ag-Au deposit.

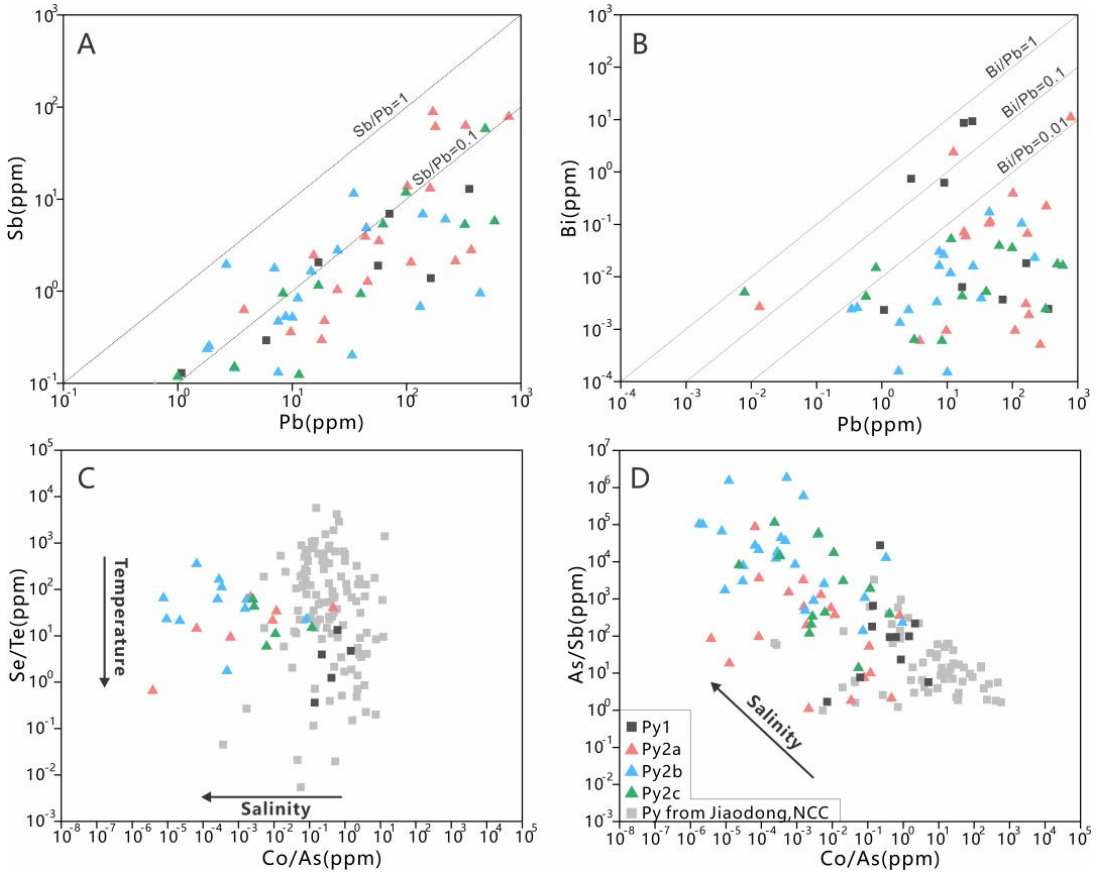

Figure 11. Bivariate plots of trace element for pyrite from Niujuan Ag-Au deposit and Au-only deposits from Jiaodong Province. Data source for Jiaodong are from [10,84]. (**A**) Sb-Pb; (**B**) Bi-Pb; (**C**) Se/Te-Co/As; (**D**) As/Sb-Co/As.

5.3. Genesis of Ore Deposit

The North China Craton (NCC) is one of the world's most important gold provinces. The giant gold endowment of Jiaodong Province, which hosts the largest gold resources and reserves in the NCC, formed at ~120 ± 5 Ma in response to intense lithospheric thinning of the craton [4]. In contrast, vein-type Au deposits in the northern NCC are commonly enriched in Ag and Te, as exemplified by the Dongping Au-Te deposit and the Niujuan Ag-Au deposit. Garnet U-Pb and fluorite Sm-Nd geochronology constrain the mineralization ages of these deposits to ~142 ± 5 Ma and 139.2 ± 3.8 Ma, respectively [7,27], indicating that they formed mainly during retrogressive extension following the westward subduction of the Paleo-Pacific plate [85]. The zircon U-Pb age of the wall rocks is 268.7 ± 3.2 Ma, which is much older than the mineralization age of the Niujuan deposit. Relatively consistent sulfur isotopes in the range of 3.8–6.7‰ suggest a dominant magmatic sulfur source. And H-O isotopes showing mineralization is associated with magmatic–hydrothermal fluids with variable contributions from meteoric water. Furthermore, orogenic Au deposits are generally characterized by low base metal contents, whereas the Niujuan deposit is distinguished by an Ag-Au-Pb-Zn mineralization association, indicating that the Niujuan deposit should be the product of magmatic–hydrothermal forces.

The Niujuan Ag-Au deposit is structurally controlled by NE-trending fracture zones [86,87]. Widespread sericite alteration and sulfide mineralization (Figure 4F,G), together with homogenization temperatures of 230–310 °C [86], indicate that the ore-forming fluids were near-neutral to weakly acidic. Experimental studies suggest that in low-to-medium-temperature hydrothermal systems, Au is transported predominantly as $Au(HS)_2^-$, $Au(HS)^0$, $HAu(HS)_2^0$, and $Au_2(HS)_2S^{2-}$ complexes [88], whereas Ag oc-

curs mainly as Ag^+ and is transported as hydrosulfide ($AgHS^0$) and chloride ($AgCl_2^-$) complexes [89]. The widespread occurrence of sulfides (e.g., pyrite) in the wall rocks, together with evidence for fluid immiscibility recorded by coexisting immiscible fluid inclusions [26,84], porous pyrite textures, and abundant electrum occurring along fractures or as inclusions, indicates that sulfidation and fluid boiling were the primary mechanisms responsible for Au-Ag precipitation. The relatively high pyrite Bi/Pb (e.g., >0.1) and Sb/Pb (e.g., >0.01) ratios at Niujuan also support that the ore-formation fluid underwent vigorous-to-moderate boiling (Figure 11A,B) because Pb is not preferentially transported by uprising hydrothermal fluids after boiling in comparison to Sb and Bi [90]. Generally, decreases in the Se/Te ratio in pyrite have been suggested to reflect fluid cooling [91]. At the Niujuan locality, the vast majority of Se/Te ratios are lower than <356.9, with a median value of 22.0, when two outliers are excluded. This geochemical signature, observed across the Py1 to Py2 paragenetic stages, indicates that the temperature variation during Au and Ag precipitation was not statistically significant (Figure 11C). In addition, vapor-rich fluids should be characterized by lower Co/As and higher As/Sb ratios relative to the residual liquid [91]. Consequently, the decreased Co/As ratios and negative correlation between Co/As and As/Sb ratios in the Niujuan pyrite (Figure 11D) further support the explanation of decreasing fluid salinities induced by the vapor–liquid fraction at deeper levels [90,91].

6. Conclusions

(1) Pyrite from the main mineralization stage of the Niujuan deposit contains low concentrations of invisible gold, with an average of 1.4 ppm, whereas silver contents are significantly higher, averaging 38 ppm. The combined effects of wall-rock sulfidation and fluid boiling are interpreted to have played a key role in promoting Au-Ag precipitation.

(2) The Ag-Au deposits in the northern North China Craton, exemplified by the Niujuan deposit, formed during the Yanshanian period in response to the rollback of the Paleo-Pacific plate. Mineralization is associated with magmatic–hydrothermal fluids with variable contributions from meteoric water. These deposits formed earlier than the Au-only deposits in Jiaodong Province, and differences in formation depth are inferred to have been a primary factor controlling the contrasting ore-forming fluid compositions.

Author Contributions: Conceptualization and methodology, R.C., W.L., and X.L.; validation, R.C.; formal analysis, W.L.; investigation, R.C., L.C., W.L., K.H., W.P., W.C., and C.L.; resources, X.L. and K.H.; data curation, X.L.; writing—original draft preparation, W.L. and X.L.; writing—review and editing, R.C.; funding acquisition, R.C. and L.C. All authors have read and agreed to the published version of the manuscript.

Funding: This research was funded by the Mineralization Patterns of the Northern Hebei Yingfang-Niujuan Polymetallic Deposit Project (Grant No.: 13000024P0069B410315Q) and the National Natural Science Foundation of China (Grant No.: 42272073).

Data Availability Statement: The original contributions presented in this study have been included in the article. Further inquiries can be directed to the corresponding authors.

Acknowledgments: We gratefully acknowledge the invaluable support and assistance provided by Hui Zhang, Yucheng Gong, Zhen Zhao, and Chuan Yang Luo during fieldwork.

Conflicts of Interest: Chunlai Liu, Ruiming Cao, Wei Pan, Wei Cui and Linan Cui are employees of The Second Geological Brigade of Hebei Bureau of Geology and Mineral Exploration and Development. The authors declare that they have no known competing financial interests or personal relationships that could have appeared to influence the work reported in this paper.

References

1. Zhai, M.G. Formation, Tectonic evolution and metallogenesis of North China Craton. *Miner. Depos. Geol.* **2010**, *29*, 24–36. [CrossRef]
2. Qin, K.Z.; Han, R.; Hui, K.X.; Li, Z.; Kan, Q.; Wang, L.; Gao, S.; Zhao, J.X. Types, spatial-temporal distribution, and exploration potential of silver deposits in China. *Acta Petrol. Sin.* **2025**, *41*, 383–415. [CrossRef]
3. Zhang, L.C.; Bai, Y.; Zhu, M.T.; Huang, K. Regional Differences of Au deposits on the North China Craton. *Acta Geol. Geophys. Sin.* **2018**, *40*, 363–380.
4. Deng, J.; Wang, Q.; Zhang, L.; Xue, S.; Liu, X.; Yang, L.; Yang, L.; Qiu, K.; Liang, Y. Metallogenetic model of Jiaodong-type Au deposits, eastern China. *Earth Sci.* **2023**, *66*, 2287–2310. [CrossRef]
5. Bao, Z.; Sun, W.; Li, C.; Zhao, Z. U-Pb dating of hydrothermal zircon from the Dongping gold deposit in North China: Constraints on the mineralization processes. *Ore Geol. Rev.* **2014**, *61*, 107–119. [CrossRef]
6. Wang, D.Z.; Liu, J.; Zhai, D.G.; Zhen, S.M.; Wang, J. Study on molybdenite Re-Os and zircon U-Pb ages of the Dongping tellurium-gold deposit in Hebei Province. *Front. Earth Sci.* **2020**, *27*, 405–419. [CrossRef]
7. Fan, G.H.; Li, J.W.; Deng, X.D.; Gao, W.S.; Li, S.Y. Age and origin of the Dongping Au-Te deposit in the North China Craton revisited: Evidence from paragenesis, geochemistry, and in situ U-Pb geochronology of garnet. *Econ. Geol.* **2021**, *116*, 963–985. [CrossRef]
8. Mills, S.E.; Tomkins, A.G.; Weinberg, R.F.; Fan, H.R. Implications of pyrite geochemistry for gold mineralisation and remobilisation in the Jiaodong gold district, northeast China. *Ore Geol.* **2015**, *71*, 150–168. [CrossRef]
9. Ye, T.; Li, N. The application of pyrite LA-ICP-MS trace element analysis to Au deposits. *Geol. Sci.* **2015**, *50*, 1178–1199.
10. Yang, L.Q.; Deng, J.; Wang, Z.L.; Guo, L.N.; Li, R.H.; Groves, D.I.; Danyushevsky, L.V.; Zhang, C.; Zheng, X.L.; Zhao, H. Relationships between gold and pyrite at the Xincheng gold deposit, Jiaodong Peninsula, China: Implications for gold source and deposition in a brittle epizonal environment. *Econ. Geol.* **2016**, *111*, 105–126. [CrossRef]
11. Fan, H.R.; Li, X.H.; Zuo, Y.B.; Chen, L.; Liu, S.; Hu, F.; Feng, K. In-situ LA-(MC)-ICPMS and (Nano) SIMS trace elements and sulfur isotope analyses on sulfides and application to confine metallogenic process of ore deposit. *Acta Petrol. Sin.* **2018**, *34*, 3479–3496.
12. Zhang, H.Y.; Zhao, Q.; Zhao, G.; Hong, J.X.; Liu, J.; Zhai, D.G. In situ LA-ICP-MS trace element analysis of pyrite and its application in study of Au deposit. *Miner. Depos. Geol.* **2022**, *41*, 1182–1199. [CrossRef]
13. Xiao, J.; Xie, Z.; Xia, Y.; Lan, T.; Zhang, L.; Pan, L.; Hu, H.; Wang, H.; Tan, Q.; Xu, Y. Predominant fracture gold in the Jiaodong gold province, China: Constraints on gold mineralization processes. *Ore Geol. Rev.* **2024**, *165*, 105915. [CrossRef]
14. Fan, H.; Lan, T.; Li, X.; Santosh, M.; Yang, K.; Hu, F.; Feng, K.; Hu, H.; Peng, H.; Zhang, Y. Conditions and processes leading to large-scale gold deposition in the Jiaodong province, eastern China. *Sci. China Earth Sci.* **2021**, *51*, 1504–1523. [CrossRef]
15. Li, X.H.; Fan, H.R.; Yang, K.F.; Hollings, P.; Liu, X.; Hu, F.F.; Cai, Y.C. Pyrite textures and compositions from the Zhuangzi Au deposit, southeastern North China Craton: Implication for ore-forming processes. *Contrib. Mineral. Petrol.* **2018**, *173*, 73. [CrossRef]
16. Fan, H.R.; Xie, Y.H.; Wang, Y.L. The properties of magmatic hydrothermal fluid of huashan granitic batholith in western henan province and their relationship to gold mineralization. *Acta Petrol. Sin.* **1993**, *9*, 136–145.
17. Fan, H.R.; Xie, Y.H.; Zheng, X.Z.; Wang, Y.L. Ore-forming fluids in hydrothermal breccia-related gold mineralization in Qiyugou, Henan Province. *Acta Petrol. Sin.* **2000**, *16*, 559–563.
18. Fan, H.R.; Xie, Y.H.; Zhai, M.G.; Jin, C.W. A three stage fluid flow model for Xiaoqinling lode gold metallogenesis in the Henan and Shaanxi provinces, central China. *Acta Petrol. Sin.* **2003**, *19*, 260–266. [CrossRef]
19. Mao, J.; He, Y.; Ding, T. Carbon, Mantle Fluids Involved in Metallogenesis of Jiaodong (East Shandong) Gold District: Evidence of C, O and H Isotopes. *Miner. Depos. Geol.* **2002**, *21*, 121–128. [CrossRef]
20. Zhu, R.; Fan, H.; Li, J.; Meng, Q.; Li, S.; Zeng, Q. Decratonic Au deposits. *Sci. China Earth Sci.* **2015**, *58*, 1523–1537. [CrossRef]
21. Li, J.W.; Bi, S.J.; Selby, D.; Chen, L.; Vasconcelos, P.; Thiede, D.; Zhou, M.F.; Zhao, X.F.; Li, Z.K.; Qiu, H.N. Giant Mesozoic gold provinces related to the destruction of the North China Craton. *Earth Planet. Sci. Lett.* **2012**, *349*, 26–37. [CrossRef]
22. Chen, Y.J. Metallogenic time and tectonic setting of the Jiaodong gold province, eastern China. *Acta Petrol. Sin.* **2004**, *20*, 907–922.
23. Chen, Y.J.; Tang, G.J.; Pirajno, F.; Qi, J.P.; Lin, Z.J. Hydrothermal metallogeny of the Shanggong gold deposit, east Qinling: Radiogenic isotope geochemistry. *Miner. Rocks* **2004**, *24*, 22–27. [CrossRef]
24. Jiang, S.Y.; Dai, B.Z.; Jiang, Y.H.; Zhao, H.X.; Hou, M.L. Jiaodong and Xiaoqinling: Two orogenic gold provinces formed in different tectonic settings. *Acta Petrol. Sin.* **2009**, *25*, 2727–2738.
25. Goldfarb, R.J.; Groves, D.I. Orogenic gold: Common or evolving fluid and metal sources through time. *Lithos* **2015**, *233*, 2–26. [CrossRef]
26. Yan, X.; Chen, B.; Duan, X.; Wang, Z. Geochronology and ore genesis of the Niujuan-Yingfang Pb-Zn-Ag deposit in Fengning, Northern North China Craton: Constraints from fluid inclusions, HOS isotopes and fluorite Sr-Nd isotopes. *J. Earth Sci.* **2021**, *32*, 81–102. [CrossRef]

27. Li, Y.J.; Li, S.R.; Santosh, M.; Mo, X.; Gao, K.B.; Ma, Y. Isotope geochemistry and geochronology of the Niujuan silver deposit, northern North China Craton: Implications for magmatism and metallogeny in an extensional tectonic setting. *Ore Geol. Rev.* **2017**, *90*, 36–51. [CrossRef]
28. Zeng, Q.; Wang, Y.; Yang, J.; Guo, Y.; Yu, B.; Zhou, L.; Qiu, H. Spatial-temporal distribution and tectonic setting of gold deposits in the Northern margin gold belt of the North China Craton. *Int. Geol. Rev.* **2021**, *63*, 941–972. [CrossRef]
29. Su, R.; Sun, G.S.; Du, M.Y. Geochemical characteristics of biotites from amphibolites in JianPing Group, south-eastern Chifeng and their geological implications. *Glob. Geol.* **2015**, *34*, 307–311.
30. Dong, C.Y.; Wan, Y.S.; Zhang, Y.H.; Yang, Z.Q.; Liu, D.Y. 3.3-3.1 Ga magmatism recorded in an outcrop of the Dongshan Complex in the Anshan area, North China Craton: Evidence from geochemistry and SHRIMP zircon dating. *Acta Petrol. Sin.* **2013**, *29*, 414–420.
31. Nie, F.J.; Jiang, S.H.; Su, X.X.; Wang, X.L. Geological features and origin of gold deposits occurring in the Baotou-Bayan Obo district, south-central Inner Mongolia, People's Republic of China. *Ore Geol. Rev.* **2002**, *20*, 139–169. [CrossRef]
32. Nie, F.J. Type and distribution of gold deposits along the northern margin of the North China Craton, People's Republic of China. *Int. Geol. Rev.* **1997**, *39*, 151–180. [CrossRef]
33. Gao, M.; Gao, F. Retrogressive Metamorphism of Archean Granulites and Evidence of Rb-Sr Isochron Age in Zhangjiakou and Xuanhua Regions. *J. Hebei Coll. Geol.* **1988**, *11*, 11–19.
34. Wang, Q.C. On the age of Hongqiyingzi Group and geological thermal events in undergone. *Sci. Geol. Sin.* **1992**, *1*, 17–24.
35. Zhai, M.G. 2.1~1.7 Ga geological event group and its geotectonic significance. *Acta Petrol. Sin.* **2004**, *20*, 1343–1354.
36. Yan, X.; Chen, B.; Wang, Z.Q.; Duan, X. The Petrogenesis of the Two-Stage A-Type Granites from the Niujuan Silver Deposit in the Northern Margin of North China Craton and Their Tectonic Implications. *Acta Petrol. Sin.* **2019**, *35*, 558–588. [CrossRef]
37. Li, Y.J.; Li, S.G.; Yuan, M.W. *Thermophysical Characteristics of Pyrite in the Fengning Silver-Polymetallic Deposit, Hebei Province, and Their Indicative Significance*; China Mining Association: Beijing, China, 2023. [CrossRef]
38. Li, J.M.; Gong, E.P.; Yao, Y.Z.; Liang, J.H. The geological-geochemical characteristics and metallogeny of Fengning silver-polymetallic ore deposit, north Hebei province. *Geol. Prospect. Forum* **2006**, *4*, 241–247.
39. Li, Y.J. *Metallogenic Process and Potential of the Silver-Polymetallic System in Fengning, Northern Hebei Province: Constraint of Geochronology, Geochemistry and Genetic Mineralogy*; China University of Geosciences: Beijing, China, 2020. [CrossRef]
40. Gao, K.B. *Characteristics of Hydrogen and Oxygen Isotopes, Fluid Inclusions and Fluid Evolution of the Fengning Ag(Au) Deposit, Hebei Province: Comparing with Decratonic Au Deposits*; China University of Geosciences: Beijing, China, 2018.
41. Liu, Y.S.; Hu, Z.C.; Gao, S.; Günther, D.; Xu, J.; Gao, C.; Chen, H. In situ analysis of major and trace elements of anhydrous minerals by LA-ICP-MS without applying an internal standard. *Chem. Geol.* **2008**, *257*, 34–43. [CrossRef]
42. Crowe, D.E.; Vaughan, R.G. Characterization and use of isotopically homogeneous standards for in situ laser microprobe analysis of 34S/32S ratios. *Am. Mineral.* **1996**, *81*, 187–193. [CrossRef]
43. Clayton, R.N.; Mayeda, T.K. The Use of Bromine Pentafluoride in the Extraction of Oxygen from Oxides and Silicates for Isotopic Analysis. *Geochim. Cosmochim. Acta* **1963**, *27*, 43–52. [CrossRef]
44. Zhu, Q.; Cook, N.J.; Xie, G.; Ciobanu, C.L.; Jian, W.; Wade, B.P.; Xu, J. Gamma-enhancement of reflected light images: A rapid, effective tool for assessment of compositional heterogeneity in pyrite. *Am. Mineral.* **2021**, *106*, 497–505. [CrossRef]
45. Li, S.-S.; Li, L.; Li, S.-R.; Santosh, M.; Alam, M. The Age and Mineralization Processes of Decratonic Lode Gold Deposits in the Southern North China Craton: Constraints from Trace Elements, in-situ S-Pb Isotopes and Rb-Sr Geochronology of Pyrite from the Chen'er Gold Deposit. *Ore Geol. Rev.* **2022**, *145*, 104888. [CrossRef]
46. Tan, J.; Wei, J.; Li, Y.; Fu, L.; Li, H.; Shi, W.; Tian, N. Origin and Geodynamic Significance of Fault-Hosted Massive Sulfide Gold Deposits from the Guocheng-Liaoshang Metallogenic Belt, Eastern Jiaodong Peninsula: Rb-Sr Dating, and H-O-S-Pb Isotopic Constraints. *Ore Geol. Rev.* **2015**, *65*, 687–700. [CrossRef]
47. Mills, S.E.; Tomkins, A.G.; Weinberg, R.F.; Fan, H.-R. Anomalously Silver-Rich Vein-Hosted Mineralisation in Disseminated-Style Gold Deposits, Jiaodong Gold District, China. *Ore Geol. Rev.* **2015**, *68*, 127–141. [CrossRef]
48. Zhang, L.C.; Shen, Y.C.; Zou, W.L.; Li, H.M. Ore-Forming Geological and Geochemical Characteristics and Genesis of the Dazhuangzi Gold Deposit. *Geol. Resour.* **2002**, *11*, 16–22. [CrossRef]
49. Ma, W.-D.; Fan, H.-R.; Liu, X.; Yang, K.-F.; Hu, F.-F.; Zhao, K.; Cai, Y.-C.; Hu, H.-L. Hydrothermal Fluid Evolution of the Jintingling Gold Deposit in the Jiaodong Peninsula, China: Constraints from U-Pb Age, CL Imaging, Fluid Inclusion and Stable Isotope. *J. Asian Earth Sci.* **2018**, *160*, 287–303. [CrossRef]
50. Wang, C.M.; Deng, J.; Santosh, M.; Carranza, E.J.M. Timing, tectonic implications and genesis of gold mineralization in the Xincheng gold deposit, China: C-H-O isotopes, pyrite Rb-Sr and zircon fission track thermochronometry. *Ore Geol. Rev.* **2014**, *65*, 123–138. [CrossRef]
51. Xue, J.L.; Li, S.R.; Pang, Z.S.; Tao, W.; Sun, W.Y.; Chen, H.; Zhang, Y.Q. Ore-Forming Fluids, Sources of Materials in the Denggezhuang Gold Deposit, Jiaodong Peninsula and Implications for Ore Genesis. *Acta Petrol. Sin.* **2018**, *34*, 1453–1468.

52. Wang, Y.W. A study on hydrogen and oxygen isotope geochemistry of gold deposits in China. *J. Precious Metall. Geol.* **1993**, *2*, 169–180. [CrossRef]
53. Bi, X.; Hu, R.Z.; Peng, J.T.; Li, H.L.; Hu, X.Y. REE and HFSE Geochemical Characteristics of Pyrites in Yao'an Gold Deposit: Tracing Ore Forming Fluid Signatures. *Bull. Mineral. Petrol. Geochem.* **2004**, *23*, 1–4. [CrossRef]
54. Large, R.R.; Maslennikov, V.V.; Robert, F.; Danyushevsky, L.V.; Chang, Z. Multistage sedimentary and metamorphic origin of pyrite and gold in the giant Sukhoi Log deposit, Lena gold province, Russia. *Econ. Geol.* **2007**, *102*, 1233–1267. [CrossRef]
55. Reich, M.; Deditius, A.; Chryssoulis, S.; Li, J.W.; Ma, C.Q.; Parada, M.A.; Barra, F.; Mittermayr, F. Pyrite as a record of hydrothermal fluid evolution in a porphyry copper system: A SIMS/EMPA trace element study. *Geochim. Cosmochim. Acta* **2013**, *104*, 42–62. [CrossRef]
56. Reich, M.; Kesler, S.E.; Utsunomiya, S.; Palenik, C.S.; Chryssoulis, S.L.; Ewing, R.C. Solubility of gold in arsenian pyrite. *Geochim. Cosmochim. Acta* **2005**, *69*, 2781–2796. [CrossRef]
57. Gregory, D.D.; Large, R.R.; Halpin, J.A.; Baturina, E.L.; Lyons, T.W.; Wu, S.; Danyushevsky, L.; Sack, P.J.; Chappaz, A.; Maslennikov, V.V.; et al. Trace Element Content of Sedimentary Pyrite in Black Shales. *Econ. Geol.* **2015**, *110*, 1389–1410. [CrossRef]
58. Cook, N.; Ciobanu, C.L.; George, L.; Zhu, Z.Y.; Wade, B.; Ehrig, K. Trace Element Analysis of Minerals in Magmatic-Hydrothermal Ores by Laser Ablation Inductively-Coupled Plasma Mass Spectrometry: Approaches and Opportunities. *Minerals* **2016**, *6*, 111. [CrossRef]
59. Zhu, Z.Y.; Cook, N.J.; Yang, T.; Ciobanu, C.L.; Zhao, K.D.; Jiang, S.Y. Mapping of sulfur isotopes and trace elements in sulfides by LA-(MC)-ICP-MS: Potential analytical problems, improvements and implications. *Minerals* **2016**, *6*, 110. [CrossRef]
60. Liang, Q.L.; Xie, Z.; Song, X.Y.; Wirth, R.; Xia, Y.; Cline, J. Evolution of invisible Au in arsenian pyrite in Carlin-type Au deposits. *Econ. Geol.* **2021**, *116*, 515–526. [CrossRef]
61. Li, W.; Cook, N.J.; Xie, G.Q.; Mao, J.W.; Ciobanu, C.L.; Li, J.W.; Zhang, Z.Y. Textures and trace element signatures of pyrite and arsenopyrite from the Gutaishan Au-Sb deposit, south China. *Miner. Depos.* **2019**, *54*, 591–610. [CrossRef]
62. Loftus-Hills, G.D.; Solomon, M. Cobalt, Nickel and Selenium in Sulphides as Indicators of Ore Genesis. *Miner. Depos.* **1967**, *2*, 228–242. [CrossRef]
63. Price, B.J. Phase Relations and Mineral Assemblages in the System Fe-Co-Ni-S. *Can. Mineral.* **1972**, *11*, 759–768.
64. Bralia, A.; Sabatini, G.; Troja, F. A revaluation of the Co/Ni ratio in pyrite as geochemical tool in ore genesis problems. *Miner. Depos.* **1979**, *14*, 353–374. [CrossRef]
65. Cao, G.S.; Zhang, Y.; Chen, H. Trace elements in pyrite from orogenic Au deposits: Implications for metallogenic mechanism. *Acta Petrol. Sin.* **2023**, *39*, 2330–2346. [CrossRef]
66. Fleet, M.E.; Mumin, A.H. Gold-bearing arsenian pyrite and marcasite and arsenopyrite from Carlin Trend Au deposits and laboratory synthesis. *Am. Mineral.* **1997**, *82*, 182–193. [CrossRef]
67. Deditius, A.P.; Reich, M.; Kesler, S.E.; Utsunomiya, S.; Chryssoulis, S.L.; Walshe, J.; Ewing, R.C. The coupled geochemistry of Au and As in pyrite from hydrothermal ore deposits. *Geochim. Cosmochim. Acta* **2014**, *140*, 644–670. [CrossRef]
68. Wu, Y.F.; Fougerouse, D.; Evans, K.; Reddy, S.M.; Saxey, D.W.; Guagliardo, P.; Li, J.W. Gold, arsenic, and copper zoning in pyrite: A record of fluid chemistry and growth kinetics. *Geology* **2019**, *47*, 641–644. [CrossRef]
69. Xie, Z.; Xia, Y.; Cline, J.S.; Pribil, M.J.; Koenig, A.; Tan, Q.; Wei, D.; Wang, Z.; Yan, J. Magmatic origin for sediment-hosted Au deposits, Guizhou Province, China: In situ chemistry and sulfur isotope composition of pyrites, Shuiyindong and Jinfeng deposits. *Econ. Geol.* **2018**, *113*, 1627–1652. [CrossRef]
70. Hofstra, A.H.; Cline, J.S. Characteristics and models for Carlin type Au deposits. *Rev. Econ. Geol.* **2000**, *13*, 163–220. [CrossRef]
71. Cook, N.J.; Ciobanu, C.L.; Meria, D.; Silcock, D.; Wade, B. Arsenopyrite-pyrite association in an orogenic goldore: Tracing mineralization history from textures and trace elements. *Econ. Geol.* **2013**, *108*, 1273–1283. [CrossRef]
72. Large, R.R.; Danyushevsky, L.; Hollit, C.; Maslennikov, V.; Meffre, S.; Gilbert, S.; Bull, S.; Scott, R.; Emsbo, P.; Thomas, H.; et al. Gold and trace element zonation in pyrite using a laser imaging technique: Implications for the timing of gold in orogenic and Carlin-style sediment-hosted deposits. *Econ. Geol.* **2009**, *104*, 635–668. [CrossRef]
73. Gopon, P.; Douglas, J.O.; Auger, M.A.; Hansen, L.; Wade, J.; Cline, J.S.; Robb, L.J.; Moody, M.P. A nanoscale investigation of Carlin-type Au deposits: An atom-scale elemental and isotopic perspective. *Econ. Geol.* **2019**, *114*, 1123–1133. [CrossRef]
74. Li, W.; Cook, N.J.; Xie, G.Q.; Mao, J.W.; Ciobanu, C.L.; Fu, B. Complementary textural, trace element and isotope analysis of sulfides constrain ore-forming processes for the slate-hosted Yuhengtang Au deposit, South China. *Econ. Geol.* **2021**, *116*, 1825–1848. [CrossRef]
75. Chang, Z.; Large, R.R.; Maslennikov, V. Sulfur isotopes in sediment-hosted orogenic Au deposits: Evidence for an early timing and a seawater sulfur source. *Geology* **2008**, *36*, 971–974. [CrossRef]
76. Meffre, S.; Large, R.R.; Scott, R.; Woodhead, J.; Chang, Z.; Gilbert, S.E.; Danyushevsky, L.V.; Maslennikov, V.; Hergt, J.M. Age and pyrite Pb-isotopic composition of the giant Sukhoi Log sediment-hosted gold deposit, Russia. *Geochim. Cosmochim. Acta* **2008**, *72*, 2377–2391. [CrossRef]
77. Ohmoto, H. Stable isotope geochemistry of ore deposits: Reviews in Mineralogy and Geochemistry. *Rev. Mineral.* **1986**, *16*, 491–559.
78. Seal, R.R. Sulfur isotope geochemistry of sulfide minerals. *Rev. Mineral. Geochem.* **2006**, *61*, 633–677. [CrossRef]

79. Phillips, G.N.; Powell, R. Formation of Au deposits: A metamorphic devolatilization model. *J. Metamorph. Geol.* **2010**, *28*, 689–718. [CrossRef]
80. Hu, H.L.; Fan, H.R.; Santosh, M.; Liu, X.; Cai, Y.C.; Yang, K.F. Ore-forming processes in the Wang'ershan gold deposit (Jiaodong, China): Insight from microtexture, mineral chemistry and sulfur isotope compositions. *Ore Geol. Rev.* **2020**, *123*, 103600. [CrossRef]
81. Li, L.; Santosh, M.; Li, S.-R. The "Jiaodong Type" Gold Deposits: Characteristics, Origin and Prospecting. *Ore Geol. Rev.* **2015**, *65*, 589–611. [CrossRef]
82. Liu, F.S.; Zhang, G.H. Genesis of the Niuquan Hot-Spring Type Ag-(Au) Deposit in Hebei Province. *J. Precious Met. Geol.* **1996**, *5*, 48–58.
83. Chen, W.J.; Liu, H.T.; Zhang, D.H. Fluid inclusion's characteristics of the Niujuan silve deposit in Fengning, Hebei, and its geological significance. *Miner. Resour. Geol.* **2007**, *21*, 12–16. [CrossRef]
84. Xiao, T.T. *The Sources of Ore-Forming Materials for Gold Deposits in the Northern Margin of the North China Craton: Constraints from Hg-S Isotopes and Pyrite Trace Elements*; Jilin University: Changchun, China, 2024. [CrossRef]
85. Mao, J.; Liu, P.; Goldfarb, R.J.; Goryachev, N.A.; Pirajno, F.; Zheng, W.; Zhou, M.; Zhao, C.; Xie, G.; Yuan, S.; et al. Cretaceous large-scale metal accumulation triggered by post-subductional large-scale extension, East Asia. *Ore Geol. Rev.* **2021**, *136*, 104270. [CrossRef]
86. Wang, S.Q.; Liu, X.W. Geological characteristics and ore-controlling significance of the cryptoexploed breccia in Niujuan silver deposit Hebei Province. *Geol. Prospect. Forum* **2009**, *24*, 139–141. [CrossRef]
87. Fan, L. Geological characteristics and ore-controlling factors of Niujuanzi silver-gold deposit in Fengning County, Hebei. *Miner. Resour. Geol.* **2021**, *35*, 50–57. [CrossRef]
88. Seward, T.M. Thio complexes of gold and the transport of gold in hydrothermal ore solutions. *Geochim. Cosmochim. Acta* **1973**, *37*, 379–399. [CrossRef]
89. Stefánsson, A.; Seward, T.M. Experimental determination of the stability and stoichiometry of sulphide complexes of silver (I) in hydrothermal solutions to 400 °C. *Geochim. Cosmochim. Acta* **2003**, *67*, 1395–1413. [CrossRef]
90. Román, N.; Reich, M.; Leisen, M.; Morata, D.; Barra, F.; Deditius, A.P. Geochemical and Micro-Textural Fingerprints of Boiling in Pyrite. *Geochim. Cosmochim. Acta* **2019**, *246*, 60–85. [CrossRef]
91. Keith, M.; Haase, K.M.; Chivas, A.R.; Klemd, R. Phase Separation and Fluid Mixing Revealed by Trace Element Signatures in Pyrite from Porphyry Systems. *Geochim. Cosmochim. Acta* **2022**, *329*, 185–205. [CrossRef]

Disclaimer/Publisher's Note: The statements, opinions and data contained in all publications are solely those of the individual author(s) and contributor(s) and not of MDPI and/or the editor(s). MDPI and/or the editor(s) disclaim responsibility for any injury to people or property resulting from any ideas, methods, instructions or products referred to in the content.